Computers and Structures 164 (2016) 161–180

Contents lists available at ScienceDirect

Computers and Structures

journal homepage: www.elsevier.com/locate/compstruc

hp-Finite element solution of coupled stationary magnetohydrodynamics problems including magnetostrictive effects

D. Jin, P.D. Ledger *, A.J. Gil

Zienkiewicz Centre for Computational Engineering, College of Engineering, Swansea University Bay Campus, Swansea SA1 8EN, United Kingdom

ARTICLE INFO

Article history:
Received 14 April 2015
Accepted 8 November 2015

Keywords:
Magnetohydrodynamics
Coupled problems
hp-Finite elements
Magnetostriction

ABSTRACT

We extend our existing *hp*-finite element framework for non-conducting magnetic fluids (Jin et al., 2014) to the treatment of conducting magnetic fluids including magnetostriction effects in both two- and three-dimensions. In particular, we present, to the best of our knowledge, the first computational treatment of magnetostrictive effects in conducting fluids. We propose a consistent linearisation of the coupled system of non-linear equations and solve the resulting discretised equations by means of the Newton–Raphson algorithm. Our treatment allows the simulation of complex flow problems, with non-homogeneous permeability and conductivity, and, apart from benchmarking against established analytical solutions for problems with homogeneous material parameters, we present a series of simulations of multiphase flows in two- and three-dimensions to show the predicative capability of the approach as well as the importance of including these effects.

1. Introduction

Magnetohydrodynamics (MHD) studies the behaviour of electrically conducting fluids under the existence of a magnetic field [6,15,30]. Since it was established by Hannes Alfvén in 1942, the field of MHD has grown rapidly and is now widely established and used in a variety of research fields, such as in geophysics (e.g. [3]), space weather forecasting (e.g. [33]), plasma physics (e.g. [22]), nuclear fusion reactors (e.g. [31]), metal casting (e.g. [14]) and in the Lorentz force flowmetre [28], to name but a few.

MHD can be viewed as a particular case of coupling between magnetic fields and fluids. In general, time independent magneto-fluid coupled problems can be described by the coupling between the steady incompressible Navier–Stokes equations

$$\rho(\nabla \boldsymbol{v})\boldsymbol{v} - \nabla \cdot [[\sigma_F]] = \boldsymbol{f}, \tag{1a}$$

$$\nabla \cdot \boldsymbol{v} = 0, \tag{1b}$$

which govern the fluid flow, and the time independent Maxwell equations

$$\nabla \times \mathcal{H} = \mathcal{J}_{ext} + \mathcal{J}_{ohm}, \tag{2a}$$

$$\nabla \times \mathcal{E} = \mathbf{0}, \tag{2b}$$

$$\nabla \cdot \mathcal{B} = 0, \tag{2c}$$

$$\nabla \cdot \mathcal{D} = \rho_v, \tag{2d}$$

which govern the electromagnetic fields. In (1), ρ is the fluid density, $\boldsymbol{v}$ is the fluid velocity, $[[\sigma_F]]$ is the Cauchy stress tensor and $\boldsymbol{f}$ is total body force. Furthermore, in (2), $\mathcal{B}$ is the magnetic flux density vector, $\mathcal{D}$ is the electric flux intensity vector, $\mathcal{J}_{ext}$ is the external current source, $\mathcal{J}_{ohm}$ is the Ohmic current, ρ_v is the volume current density and $\mathcal{E}$ and $\mathcal{H}$ are the electric and magnetic field intensity vectors, respectively.

From the fluid perspective, we shall consider it to be Newtonian, with constitutive law

$$[[\sigma_F]] = -\hat{p}[[\mathbb{I}]] + 2\hat{\mu}[[\varepsilon]], \tag{3}$$

where $[[\mathbb{I}]], [[\varepsilon]]$ are the identity and strain rate tensors, respectively. Furthermore, $\hat{p}$ is the pressure and $\hat{\mu}$ is the dynamic viscosity. From the electromagnetic perspective, we consider constitutive laws of the form

$$\mathcal{B} = \mu\mathcal{H}, \quad \mathcal{J}_{ohm} = \Sigma\mathcal{E}, \quad \mathcal{D} = \epsilon\mathcal{E}, \tag{4}$$

where μ is the permeability of the material, which describes the extent of magnetisation, Σ is its conductivity and ϵ is its permittivity. Note that residual magnetism will be ignored and that, in general, μ, Σ and ϵ are tensors, in which case we denote them as $[[\mu]], [[\Sigma]]$ and $[[\epsilon]]$, respectively. For a discussion on different classes of diamagnetic, paramagnetic and non-magnetic fluids, we refer to [26].

Intrinsic to simulating MHD problems is the coupling mechanism. The existence of a magnetic field applies a magnetic body force $\boldsymbol{f}_{EM}$ (ponderomotive force) (as a contribution to $\boldsymbol{f}$) onto the

* Corresponding author.

http://dx.doi.org/10.1016/j.compstruc.2015.11.008
0045-7949/

fluid domain, which affects the fluid flow. There are several different expressions for this magnetic body force, which can be found in the literature [10–12,29,38]. All in all, the magnetic body force consists of the Lorentz force, the magnetostrictive force and the dimagnetophoretic force [10]. We follow Stratton [38] and call the combination of dimagnetophoretic and magnetostrictive forces magnetostriction. In previous research on MHD, the electromagnetic constitutive relations are usually selected as (2), with a scalar constant permeability and conductivity. Furthermore, dielectric effects and the magnetostrictive (and dimagnetophoretic) forces are neglected and only the Lorentz force is considered [1,29]. This, in turn, leads to the standard governing equations for MHD stated in Moreau [30], Davidson [6] and Armero and Simo [1]. However, when considering problems with different fluid phases [16,41], as well as problems where the induced strain rate alters the distribution of $[[\mu]]$, which in turn changes the magnetic field distribution, magnetostrictive effects become important [26,27]. This coupling mechanism is illustrated in Fig. 1. In order to include magnetostrictive effects with ease, it makes sense to revisit the governing equations for MHD and instead express the ponderomotive force $\boldsymbol{f}_{EM}$ in terms of the divergence of a stress tensor $[[\sigma_{EM}]]$

$$\boldsymbol{f}_{EM} = \nabla \cdot [[\sigma_{EM}]], \tag{5}$$

which, in turn, permits more general coupling mechanisms to be considered. In order to solve MHD problems cost-effectively, various finite element methodologies have been applied thus far. Guermond and Minev [19,20] dealt with a decoupled linear MHD problem involving electrically conducting and insulating regions by using a mixed finite element approach with nodal ($H^1(\Omega)$ conforming) finite elements for the magnetic field. It was observed that in non-convex domains with sharp edges and corners, a nodal finite element approach may fail to capture the singularities associated with these domains. Therefore, Schneebeli and Schötzau proposed a new mixed finite element for stationary incompressible MHD based on the Sobolev space $\boldsymbol{H}(\text{curl},\Omega)$ [34,36]. In [21], a weighted regularisation approach was used to solve the same equation set. In [5], Codina and Hernández-Silva present a stabilised finite element method for the stationary magneto-hydrodynamic equations based on a simple algebraic version of the subgrid scale variational concept. Houston, Schötzau and Wei applied a discontinuous Galerkin (DG) method to linearised incompressible MHD in [23]. Greif, Schötzau, Wei and Li used a DG method with divergence free velocities for incompressible MHD [18]. A $\boldsymbol{H}(\text{div})$ conforming finite element has been proposed to solve the MHD equations so that the divergence-free condition on the magnetic flux intensity vector is rigorously guaranteed [4]. However, in all of these approaches, only a simple conducting fluid with constant permeability and conductivity was considered.

Our recent work has been devoted to the application of high-order *hp*-finite element discretisations to problems involving the coupling of electromagnetism, mechanics and fluids including electrostricitive and magnetostrictive effects. In [17], a fixed point algorithm was applied to the simulation of fully coupled electrostrictive dielectric materials. Then, in [25,26], we extended our methodology to account for magnetostrictive effects in both nearly incompressible and incompressible Newtonian fluids and applied a Newton–Raphson algorithm, which exhibits quadratic convergence of the residual and exponentially fast convergence of the unknown fields. In closely related work, [32], the *hp*-finite element analysis of three-dimensional linear piezoelectric beams is also considered.

This work continues to build on these developments and presents the following novel contributions. We extend our existing *hp*-finite element framework for non-conducting magnetic fluids to the treatment of conducting magnetic fluids including magnetostriction effects in both two- and three-dimensions. In particular, we present, to the best of our knowledge, the first computational treatment of magnetostrictive effects in conducting fluids. We propose a consistent linearisation of the resulting non-linear equations and solve the resulting discretised equations by means of the Newton–Raphson algorithm. We once again employ the high order *hp*-finite element discretisation of Schöberl and Zaglmayr [35,40], but the computational complexity in the present contribution is considerably higher than in our previous work due to the requirement of compatible H^1, L_2 and $\boldsymbol{H}(\text{curl})$ conforming discretisations, which this basis set provides. The advantages of *hp*-finite elements are already outlined in [7,8,17] and thus are not discussed here.

The article is broken down into the following sections. In Section 2, the coupling approach is introduced and applied to derive the governing equations of MHD for homogeneous conducting fluids as well as for conducting magnetostrictive fluids.

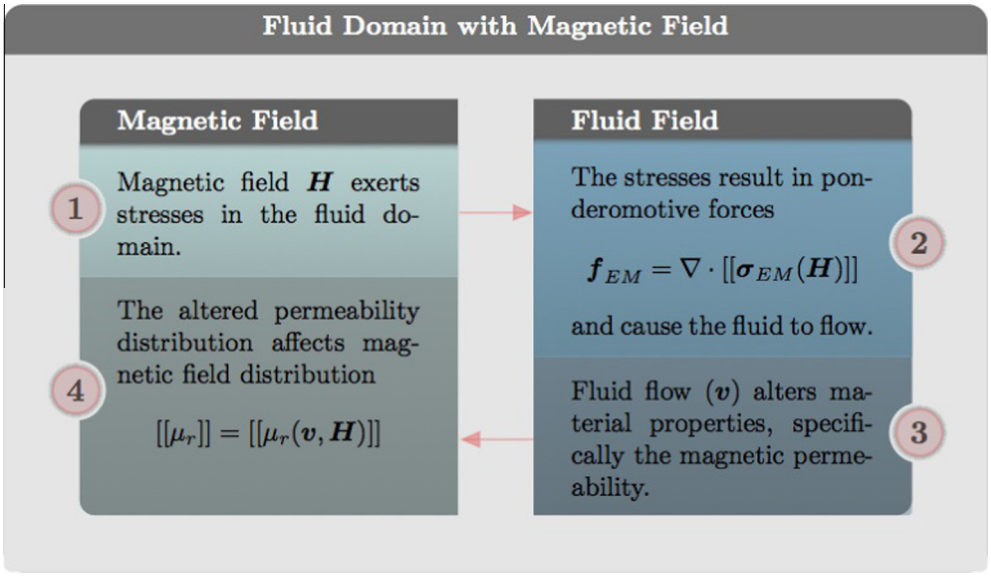

Fig. 1. Two way coupling mechanism for magnetic fields and fluids (note that $\boldsymbol{H}$ is the scaled magnetic field intensity and $\boldsymbol{v}$ is the fluid velocity introduced in Section 2.1).

In Section 3, the Newton–Raphson algorithm is established via a consistent linearisation for both cases. Section 4 describes, briefly, the main features of the *hp*-finite element framework employed for the spatial discretisation of the weak form. Section 5 includes a series of numerical examples, well known within the fluid mechanics community, which are used to demonstrate the accuracy and robustness of the *hp*-implementation. Finally, some concluding remarks are summarised in Section 6.

2. Coupling approach

In this section we construct the boundary value problems (BVPs) for describing the problem of stationary incompressible MHD, beginning with the boundary value problem for homogeneous isotropic conducting fluids with constant scalar permeability and conductivity and then, extending this to the treatment of more general magnetic fluids, including magnetostrictive effects. In the first case, following the discussion in the introduction, the electromagnetic body force is assumed to be described entirely using only the Lorentz force. Then, in the second case, we consider a more general ponderomotive force, which is expressed as the divergence of a stress tensor.

2.1. MHD for homogeneous isotropic conducting fluids

In a similar manner to [23,36], we consider a bounded Lipschitz domain $\Omega \subset \mathbb{R}^d$, $d = 2, 3, \Omega := \Omega^F \cup \Omega^M$, where Ω^F is the fluid domain and Ω^M is the magnetic domain. For simplicity, we shall assume that $\Omega = \Omega^F = \Omega^M$ and its boundary can be described as $\partial\Omega = \partial\Omega_D^F \cup \partial\Omega_N^F = \partial\Omega_D^M \cup \partial\Omega_N^M$. We introduce the scaled fields as

$$\begin{aligned} &\boldsymbol{E} = \epsilon_0^{1/2}\boldsymbol{\mathcal{E}}, \quad \boldsymbol{D} = \epsilon_0^{-1/2}\boldsymbol{\mathcal{D}}, \quad \rho_v = \epsilon_0^{-1/2}\hat{\rho}_v, \\ &\boldsymbol{H} = \mu_0^{1/2}\boldsymbol{\mathcal{H}}, \quad \boldsymbol{B} = \mu_0^{-1/2}\boldsymbol{\mathcal{B}}, \quad \boldsymbol{J} = \mu_0^{1/2}\boldsymbol{\mathcal{J}}, \end{aligned} \tag{6}$$

where ϵ_0 and μ_0 denote the permittivity and permeability of free space, respectively. It can then be shown that the coupling between (1) and (2) due to the Lorentz force, in absence of dielectric effects and the magnetostrictive forces and with constitutive relations (4) and (3), leads to the BVP formulation derived in [1,18,36], which we write in the form

$$\rho(\nabla\boldsymbol{v})\boldsymbol{v} - \nabla\cdot[[\sigma_F]] = \boldsymbol{f} \quad \text{in } \Omega, \tag{7a}$$

$$\nabla\cdot\boldsymbol{v} = 0 \quad \text{in } \Omega, \tag{7b}$$

$$[[\mu_r]]\nabla r + \nabla\times c[[\tilde{\sigma}]]^{-1}\nabla\times\boldsymbol{H} - \nabla\times(\boldsymbol{v}\times[[\mu_r]]\boldsymbol{H}) = \boldsymbol{g} \quad \text{in } \Omega, \tag{7c}$$

$$\nabla\cdot([[\mu_r]]\boldsymbol{H}) = 0 \quad \text{in } \Omega, \tag{7d}$$

$$\boldsymbol{v} = \boldsymbol{v}_D \quad \text{on } \partial\Omega_D^F, \tag{7e}$$

$$([[\sigma_F]])\boldsymbol{n} = \boldsymbol{t} \quad \text{on } \partial\Omega_N^F, \tag{7f}$$

$$\boldsymbol{n}\times\boldsymbol{H} = \boldsymbol{f}_D \quad \text{on } \partial\Omega_D^M, \tag{7g}$$

$$\boldsymbol{n}\times(c[[\tilde{\sigma}]]^{-1}\nabla\times\boldsymbol{H} + \boldsymbol{v}\times[[\mu_r]]\boldsymbol{H}) = \boldsymbol{f}_N \quad \text{on } \partial\Omega_N^M, \tag{7h}$$

where $\boldsymbol{H}$ is the scaled magnetic field intensity introduced in (6) and $\boldsymbol{g} := \nabla\times(c[[\tilde{\sigma}]]^{-1}\boldsymbol{J}^{ex})$ is a source term, $\boldsymbol{n}$ is unit outward normal vector. In addition, $[[\tilde{\sigma}]] := (\mu_0/\epsilon_0)^{1/2}[[\Sigma]]$ is the scaled electric conductivity tensor, $[[\mu_r]] := [[\mu]]/\mu_0$ is the relative permeability tensor, c is the speed of light and $\boldsymbol{J}^{ex}$ is an external current source. Here r is the Lagrange multiplier which is used to enforce (7d) [36].

The constitutive laws for this system are stated in (4) and (3) where, for the scaled fields, $[[\mu]]$ becomes $[[\mu_r]]$ and $[[\Sigma]]$ becomes $[[\tilde{\sigma}]]$. Furthermore, in the case of a homogeneous isotropic conducting fluid, $[[\mu_r]]$ and $[[\tilde{\sigma}]]$ become constant multiples of $[[\mathbb{I}]]$ and $\hat{\mu}$ adopts a constant value. Furthermore, the body force $\boldsymbol{f}$ in this case is

$$\boldsymbol{f} := \tilde{\boldsymbol{f}} + \boldsymbol{f}_{EM} = \tilde{\boldsymbol{f}} + \nabla\times\boldsymbol{H}\times([[\mu_r]]\boldsymbol{H}), \tag{8}$$

which follows from rescaling the Lorentz force $\boldsymbol{\mathcal{J}}\times\boldsymbol{\mathcal{B}}$. In the above, $\tilde{\boldsymbol{f}}$ is the non-magnetic part of the total body force. Note that, compared to the form of the stationary incompressible MHD equations presented in [23,36], we have chosen to write the formulation in terms of the scaled magnetic intensity $\boldsymbol{H}$, rather than the magnetic flux density $\boldsymbol{\mathcal{B}} := [[\mu]]\boldsymbol{\mathcal{H}}$.

2.2. MHD for magnetostrictive conducting fluids

With the addition of suitable transmission conditions, (7) can already treat problems involving subdomains in which $[[\mu_r]]$ and $[[\tilde{\sigma}]]$ are different scalar multiples of $[[\mathbb{I}]]$. However, we also wish to include other effects. As stated in the introduction, magnetostrictive effects become crucial in the case of multiphase problems where the magnetic permeability exhibits changes in its gradient. In order to include these effects, we consider a total body force acting on the fluid domain, where we express $\boldsymbol{f}_{EM}$ in terms of the divergence of a stress tensor as

$$\boldsymbol{f} := \tilde{\boldsymbol{f}} + \nabla\cdot[[\sigma_{EM}]],$$

and, in general,

$$\begin{aligned} [[\sigma_{EM}]] &:= [[\sigma_E]] + [[\sigma_H]], \quad [[\sigma_E]] = [[\sigma_E]]_0 + [[\sigma_E]]_\epsilon, \\ [[\sigma_H]] &= [[\sigma_H]]_0 + [[\sigma_H]]_\mu. \end{aligned}$$

Note that $\boldsymbol{f}_{EM}$ expressed in this form implicitly includes the effects described by $\boldsymbol{J}\times\boldsymbol{B} = \nabla\times\boldsymbol{H}\times([[\mu]]\boldsymbol{H})$ in the absence of magnetostriction. In our case, only magnetic effects are important and so $[[\sigma_{EM}]] = [[\sigma_H]]$ and the contributions $[[\sigma_H]]_0$ and $[[\sigma_H]]_\mu$ are those associated with free space and a magnetic material, respectively. Specifically, in the case of a homogeneous isotropic medium with $[[\mu]] = \mu_0\mu_r[[\mathbb{I}]]$, then in the same manner as [17],

$$[[\sigma_H]]_0 = \mu_0\boldsymbol{\mathcal{H}}\otimes\boldsymbol{\mathcal{H}} - \frac{\mu_0}{2}(\boldsymbol{\mathcal{H}}\cdot\boldsymbol{\mathcal{H}})[[\mathbb{I}]], \tag{9a}$$

$$[[\sigma_H]]_\mu = \mu_0\left(\left((\mu_r-1) - \frac{\mu_r^{(1)}}{2}\right)\boldsymbol{\mathcal{H}}\otimes\boldsymbol{\mathcal{H}} - \frac{1}{2}((\mu_r-1) + \mu_r^{(2)})(\boldsymbol{\mathcal{H}}\cdot\boldsymbol{\mathcal{H}})[[\mathbb{I}]]\right), \tag{9b}$$

where $\mu_r^{(1)}$ and $\mu_r^{(2)}$ are as defined in [26].

Further simplifications can be made by making use of the scaled magnetic intensity $\boldsymbol{H}$, such that

$$[[\sigma_H]]_0 = \boldsymbol{H}\otimes\boldsymbol{H} - \frac{1}{2}(\boldsymbol{H}\cdot\boldsymbol{H})[[\mathbb{I}]], \tag{10a}$$

$$[[\sigma_H]]_\mu = \left((\mu_r-1) - \frac{\mu_r^{(1)}}{2}\right)\boldsymbol{H}\otimes\boldsymbol{H} - \frac{1}{2}((\mu_r-1) + \mu_r^{(2)})(\boldsymbol{H}\cdot\boldsymbol{H})[[\mathbb{I}]]. \tag{10b}$$

For a magnetostrictive conducting fluid, the stress tensor can be expressed in a similar way to [26] to include magnetostrictive effects as

$$\begin{aligned} [[\sigma_{EM}]] &= [[\sigma_H(\boldsymbol{H})]] \\ &= \left(\mu_r - \frac{\mu_r^{(1)}}{2}\right)\boldsymbol{H}\otimes\boldsymbol{H} - \frac{1}{2}(\mu_r + \mu_r^{(2)})(\boldsymbol{H}\cdot\boldsymbol{H})[[\mathbb{I}]], \end{aligned} \tag{11}$$

$$\begin{aligned} [[\mu_r]] &= [[\mu_r(\boldsymbol{v})]] \\ &= \mu_r([[\mathbb{I}]] + (\nabla\cdot\boldsymbol{v})[[\mathbb{I}]] - 2[[\varepsilon(\boldsymbol{v})]]) + \mu_r^{(1)}[[\varepsilon(\boldsymbol{v})]] \\ &\quad + \mu_r^{(2)}(\nabla\cdot\boldsymbol{v})[[\mathbb{I}]]. \end{aligned} \tag{12}$$

Using the stress tensor approach allows us to consider a more general set of boundary conditions for (7) as

$$\boldsymbol{v} = \boldsymbol{v}_D \quad \text{on } \partial\Omega_D^F,$$
$$([[\sigma_F]] + [[\sigma_{EM}]])\boldsymbol{n} = \boldsymbol{t} \quad \text{on } \partial\Omega_N^F,$$
$$\boldsymbol{n} \times \boldsymbol{H} = \boldsymbol{f}_D \quad \text{on } \partial\Omega_D^M,$$
$$\boldsymbol{n} \times (c[[\tilde{\sigma}]]^{-1}\nabla \times \boldsymbol{H} + \boldsymbol{v} \times [[\mu_r]]\boldsymbol{H}) = \boldsymbol{f}_N \quad \text{on } \partial\Omega_N^M,$$

where $\partial\Omega = \partial\Omega_D^F \cup \partial\Omega_N^F = \partial\Omega_D^M \cup \partial\Omega_N^M$ and, in general we do not require that $\partial\Omega_D^F = \partial\Omega_D^M$ or $\partial\Omega_N^F = \partial\Omega_N^M$. The difference between the homogeneous isotropic conducting fluid and a magnetostrictive conducting fluid is that, the Neumann boundary for the fluid domain contains the total stress tensor, which is more realistic at describing the actual physics since, in real experiments, terms making up the contributions to the applied traction cannot be identified separately.

If Ω consists of a series of non-overlapping regions such that $\Omega = \Omega_1 \cup \Omega_2 \cup \cdots$ then, at the interfaces between different materials, $\partial\Omega_i \cap \partial\Omega_j$, the following conditions are required to hold

$$\boldsymbol{v}|_{\partial\Omega_i} = \boldsymbol{v}|_{\partial\Omega_j}$$
$$([[\sigma_F]] + [[\sigma_{EM}]])\boldsymbol{n}|_{\partial\Omega_i} = ([[\sigma_F]] + [[\sigma_{EM}]])\boldsymbol{n}|_{\partial\Omega_j}$$
$$\boldsymbol{n} \times \boldsymbol{H}|_{\partial\Omega_i} = \boldsymbol{n} \times \boldsymbol{H}|_{\partial\Omega_j}$$
$$\boldsymbol{n} \times (c[[\tilde{\sigma}]]^{-1}\nabla \times \boldsymbol{H} + \boldsymbol{v} \times [[\mu_r]]\boldsymbol{H})|_{\partial\Omega_i} = \boldsymbol{n} \times (c[[\tilde{\sigma}]]^{-1}\nabla \times \boldsymbol{H} + \boldsymbol{v} \times [[\mu_r]]\boldsymbol{H})|_{\partial\Omega_j}.$$

3. The linearised schemes

In this section, we present the linearised schemes for both homogeneous isotropic conducting and magnetostrictive conducting fluids. Once the linearised schemes have been established by computing directional derivatives, the Newton–Raphson is applied and the resulting algorithms are summarised in Algorithms 1 and 2.

3.1. MHD for homogeneous isotropic conducting fluids

We begin by following the treatment described in Section 2.1. Associated with (7), we define for the weak solutions $(\boldsymbol{v}, \hat{p}, \boldsymbol{H}, r) \in \boldsymbol{W}(\boldsymbol{v}_D) \times Z \times \boldsymbol{Y}(\boldsymbol{f}_D) \times X$ the associated residuals $\mathcal{R}_v, \mathcal{R}_{\hat{p}}, \mathcal{R}_H$ and $\mathcal{R}_r$ as

$$\begin{aligned}\mathcal{R}_v(\boldsymbol{v}^\delta; \boldsymbol{v}, \hat{p}, \boldsymbol{H}) := &\int_\Omega \rho(\nabla\boldsymbol{v})\boldsymbol{v}\cdot\boldsymbol{v}^\delta\,\mathrm{d}\Omega + \int_\Omega [[\sigma_F]] : [[\varepsilon(\boldsymbol{v}^\delta)]]\,\mathrm{d}\Omega \\ &- \int_\Omega \tilde{\boldsymbol{f}}\cdot\boldsymbol{v}^\delta\,\mathrm{d}\Omega + \int_\Omega \boldsymbol{v}^\delta \times ([[\mu_r]]\boldsymbol{H})\cdot\nabla\times\boldsymbol{H}\,\mathrm{d}\Omega \\ &- \int_{\partial\Omega_N^F} \boldsymbol{t}\cdot\boldsymbol{v}^\delta\,\mathrm{d}\partial\Omega, \end{aligned} \tag{13a}$$

$$\mathcal{R}_{\hat{p}}(\hat{p}^\delta; \boldsymbol{v}) := \int_\Omega (\nabla\cdot\boldsymbol{v})\hat{p}^\delta\,\mathrm{d}\Omega, \tag{13b}$$

$$\begin{aligned}\mathcal{R}_H(\boldsymbol{H}^\delta; \boldsymbol{v}, \boldsymbol{H}, r) := &-\int_\Omega c[[\tilde{\sigma}]]^{-1}\nabla\times\boldsymbol{H}\cdot\nabla\times\boldsymbol{H}^\delta\,\mathrm{d}\Omega \\ &+ \int_\Omega \boldsymbol{v}\times([[\mu_r]]\boldsymbol{H})\cdot\nabla\times\boldsymbol{H}^\delta\,\mathrm{d}\Omega - \int_\Omega [[\mu_r]]\nabla r\cdot\boldsymbol{H}^\delta\,\mathrm{d}\Omega \\ &+ \int_\Omega \boldsymbol{g}\cdot\boldsymbol{H}^\delta\,\mathrm{d}\Omega - \int_{\partial\Omega_N^M}\boldsymbol{f}_N\cdot\boldsymbol{H}^\delta\,\mathrm{d}\partial\Omega, \end{aligned} \tag{13c}$$

$$\mathcal{R}_r(r^\delta; \boldsymbol{H}) := -\int_\Omega [[\mu_r]]\boldsymbol{H}\cdot\nabla r^\delta\,\mathrm{d}\Omega, \tag{13d}$$

for all $(\boldsymbol{v}^\delta, \hat{p}^\delta, \boldsymbol{H}^\delta, r^\delta) \in \boldsymbol{W}(\boldsymbol{0}) \times Z \times \boldsymbol{Y}(\boldsymbol{0}) \times X$ where, following [36], we have

$$\boldsymbol{W}(\boldsymbol{v}_D) := \left\{\boldsymbol{v} \in (H^1(\Omega))^d : \boldsymbol{v} = \boldsymbol{v}_D \text{ on } \partial\Omega\right\},$$
$$Z := \left\{\hat{p} \in L_2(\Omega) : \int_\Omega \hat{p}\,\mathrm{d}\Omega = 0\right\},$$
$$\boldsymbol{Y}(\boldsymbol{f}_D) := \{\boldsymbol{H} \in \boldsymbol{H}(\mathrm{curl},\Omega) : \boldsymbol{n}\times\boldsymbol{H} = \boldsymbol{f}_D \text{ on } \partial\Omega\},$$
$$X := \left\{r \in H^1(\Omega) : r = 0 \text{ on } \partial\Omega\right\}.$$

In the above $H^1(\Omega), L_2(\Omega), \boldsymbol{H}(\mathrm{curl},\Omega)$ have their usual meanings (e.g. [7]) and we denote by $(\boldsymbol{u},\boldsymbol{v})_\Omega := \int_\Omega \boldsymbol{u}\cdot\boldsymbol{v}\,\mathrm{d}\Omega$ the standard L_2 inner product and by $\|\boldsymbol{u}\|_{L_2} := (\boldsymbol{u},\boldsymbol{u})_\Omega^{-1/2}$ the L_2 norm. In addition, we associate the corresponding $\|u\|_{H^1} := (\|u\|_{L_2}^2 + \|\nabla u\|_{L_2}^2)^{1/2}$ and $\|\boldsymbol{u}\|_{\boldsymbol{H}(\mathrm{curl})} := (\|\boldsymbol{u}\|_{L_2}^2 + \|\nabla\times\boldsymbol{u}\|_{L_2}^2)^{1/2}$ norms.

The residuals given in (13) are obtained by weighting Eq. (7) with the weights $\boldsymbol{v}^\delta, \hat{p}^\delta, \boldsymbol{H}^\delta$ and r^δ and performing integration by parts. Notice that all boundary terms disappear for the pure Dirichlet case.

We remark that it is necessary to add the criteria that $\int_\Omega \hat{p}\,\mathrm{d}\Omega = 0$ in Z in order to ensure uniqueness of the pressure field when dealing with pure Dirichlet boundary conditions for $\boldsymbol{v}$ [37].

With an iterative solution approach in mind, we consider possible trial solutions $(\boldsymbol{v}^{[m]}, \hat{p}^{[m]}, \boldsymbol{H}^{[m]}, r^{[m]}) \in \boldsymbol{W}(\boldsymbol{v}_D) \times Z \times \boldsymbol{Y}(\boldsymbol{f}_D) \times X$ and linearise the residuals (13) as follows

$$\begin{aligned}&\mathcal{R}_v(\boldsymbol{v}^\delta; \boldsymbol{v}^{[m]}, \hat{p}^{[m]}, \boldsymbol{H}^{[m]}) + \mathcal{DR}_v(\boldsymbol{v}^\delta; \boldsymbol{v}^{[m]}, \hat{p}^{[m]}, \boldsymbol{H}^{[m]})[\boldsymbol{\delta}_v^{[m]}] \\ &+ \mathcal{DR}_v(\boldsymbol{v}^\delta; \boldsymbol{v}^{[m]}, \hat{p}^{[m]}, \boldsymbol{H}^{[m]})[\boldsymbol{\delta}_{\hat{p}}^{[m]}] + \mathcal{DR}_v(\boldsymbol{v}^\delta; \boldsymbol{v}^{[m]}, \hat{p}^{[m]}, \boldsymbol{H}^{[m]})[\boldsymbol{\delta}_H^{[m]}] = 0, \end{aligned} \tag{14a}$$

$$\mathcal{R}_{\hat{p}}(\hat{p}^\delta; \boldsymbol{v}^{[m]}) + \mathcal{DR}_{\hat{p}}(\hat{p}^\delta; \boldsymbol{v}^{[m]}[\boldsymbol{\delta}_v^{[m]}] = 0, \tag{14b}$$

$$\begin{aligned}&\mathcal{R}_H(\boldsymbol{H}^\delta; \boldsymbol{v}^{[m]}, \boldsymbol{H}^{[m]}, r^{[m]}) + \mathcal{DR}_H(\boldsymbol{H}^\delta; \boldsymbol{v}^{[m]}, \boldsymbol{H}^{[m]}, r^{[m]})[\boldsymbol{\delta}_H^{[m]}] \\ &+ \mathcal{DR}_H(\boldsymbol{H}^\delta; \boldsymbol{v}^{[m]}, \boldsymbol{H}^{[m]}, r^{[m]})[\boldsymbol{\delta}_v^{[m]}] + \mathcal{DR}_H(\boldsymbol{H}^\delta; \boldsymbol{v}^{[m]}, \boldsymbol{H}^{[m]}, r^{[m]})[\boldsymbol{\delta}_r^{[m]}] = 0, \end{aligned} \tag{14c}$$

$$\mathcal{R}_r(r^\delta; \boldsymbol{H}^{[m]}) + \mathcal{DR}_r(r^\delta; \boldsymbol{H}^{[m]})[\boldsymbol{\delta}_H^{[m]}] = 0, \tag{14d}$$

for all $(\boldsymbol{v}^\delta, \hat{p}^\delta, \boldsymbol{H}^\delta, r^\delta) \in \boldsymbol{W}(\boldsymbol{0}) \times Z \times \boldsymbol{Y}(\boldsymbol{0}) \times X$ with update equations

$$\boldsymbol{v}^{[m+1]} = \boldsymbol{v}^{[m]} + \boldsymbol{\delta}_v^{[m]}, \tag{15a}$$
$$\hat{p}^{[m+1]} = \hat{p}^{[m]} + \delta_{\hat{p}}^{[m]}, \tag{15b}$$
$$\boldsymbol{H}^{[m+1]} = \boldsymbol{H}^{[m]} + \boldsymbol{\delta}_H^{[m]}, \tag{15c}$$
$$r^{[m+1]} = r^{[m]} + \delta_r^{[m]}. \tag{15d}$$

The directional derivatives can be computed as

$$\begin{aligned}\mathcal{DR}_v(\boldsymbol{v}^\delta; \boldsymbol{v}^{[m]}, \hat{p}^{[m]}, \boldsymbol{H}^{[m]})[\boldsymbol{\delta}_v^{[m]}] = &\int_\Omega \hat{\mu}\nabla\boldsymbol{\delta}_v^{[m]} : \nabla\boldsymbol{v}^\delta\,\mathrm{d}\Omega \\ &+ \int_\Omega \hat{\mu}(\nabla\cdot\boldsymbol{\delta}_v^{[m]})(\nabla\cdot\boldsymbol{v}^\delta)\,\mathrm{d}\Omega \\ &+ \int_\Omega \rho(\boldsymbol{v}^{[m]}\cdot\nabla\boldsymbol{\delta}_v^{[m]})\cdot\boldsymbol{v}^\delta\,\mathrm{d}\Omega \\ &+ \underline{\int_\Omega \rho(\boldsymbol{\delta}_v^{[m]}\cdot\nabla\boldsymbol{v}^{[m]})\cdot\boldsymbol{v}^\delta\,\mathrm{d}\Omega}, \end{aligned} \tag{16a}$$

$$\mathcal{DR}_v(\boldsymbol{v}^\delta; \boldsymbol{v}^{[m]}, \hat{p}^{[m]}, \boldsymbol{H}^{[m]})[\boldsymbol{\delta}_{\hat{p}}^{[m]}] = -\int_\Omega (\nabla\cdot\boldsymbol{v}^\delta)\delta_{\hat{p}}^{[m]}\,\mathrm{d}\Omega, \tag{16b}$$

$$\mathcal{DR}_v(\boldsymbol{v}^\delta;\boldsymbol{v}^{[m]},\hat{p}^{[m]},\boldsymbol{H}^{[m]})[\boldsymbol{\delta}_H^{[m]}] = \underline{\int_\Omega (\boldsymbol{v}^\delta \times [[\mu_r]]\boldsymbol{\delta}_H^{[m]})\cdot\nabla\times\boldsymbol{H}^{[m]}\,\mathrm{d}\Omega} + \int_\Omega (\boldsymbol{v}^\delta\times[[\mu_r]]\boldsymbol{H}^{[m]})\cdot\nabla\times\boldsymbol{\delta}_H^{[m]}\,\mathrm{d}\Omega, \quad (16c)$$

$$\mathcal{DR}_{\hat{p}}(\hat{p}^\delta;\boldsymbol{v}^{[m]})[\boldsymbol{\delta}_v^{[m]}] = -\int_\Omega (\nabla\cdot\boldsymbol{\delta}_v^{[m]})p^\delta\,\mathrm{d}\Omega, \quad (16d)$$

$$\mathcal{DR}_H(\boldsymbol{H}^\delta;\boldsymbol{v},\boldsymbol{H},r)[\boldsymbol{\delta}_H^{[m]}] = -\int_\Omega c[[\tilde{\sigma}]]^{-1}\nabla\times\boldsymbol{\delta}_H^{[m]}\cdot\nabla\times\boldsymbol{H}^\delta\,\mathrm{d}\Omega + \underline{\int_\Omega \boldsymbol{v}^{[m]}\times([[\mu_r]]\boldsymbol{\delta}_H^{[m]})\cdot\nabla\times\boldsymbol{H}^\delta\,\mathrm{d}\Omega}, \quad (16e)$$

$$\mathcal{DR}_H(\boldsymbol{H}^\delta;\boldsymbol{v},\boldsymbol{H},r)[\boldsymbol{\delta}_v^{[m]}] = \int_\Omega (\boldsymbol{\delta}_v^{[m]}\times[[\mu_r]]\boldsymbol{H}^{[m]})\cdot\nabla\times\boldsymbol{H}^\delta\,\mathrm{d}\Omega, \quad (16f)$$

$$\mathcal{DR}_H(\boldsymbol{H}^\delta;\boldsymbol{v},\boldsymbol{H},r)[\boldsymbol{\delta}_r^{[m]}] = -\int_\Omega [[\mu_r]]\nabla\delta_r^{[m]}\cdot\boldsymbol{H}^\delta, \quad (16g)$$

$$\mathcal{DR}_r(r^\delta;\boldsymbol{H})[\boldsymbol{\delta}_H^{[m]}] = -\int_\Omega [[\mu_r]]\boldsymbol{\delta}_H^{[m]}\cdot\nabla r^\delta\,\mathrm{d}\Omega. \quad (16h)$$

where certain terms have been highlighted for later reference. Assuming the solutions $(\boldsymbol{v}^{[m]},\hat{p}^{[m]},\boldsymbol{H}^{[m]},r^{[m]})$ to be known, and associating the bilinear forms $\mathcal{C}_{vv},\mathcal{C}_{v\hat{p}},\mathcal{C}_{vH},\mathcal{C}_{\hat{p}v},\mathcal{C}_{HH},\mathcal{C}_{Hv},\mathcal{C}_{Hr}$ and $\mathcal{C}_{rH}$ in turn with the directional derivatives stated above, the Newton–Raphson iteration can be stated as: Find $(\boldsymbol{\delta}_v^{[m]},\delta_{\hat{p}}^{[m]},\boldsymbol{\delta}_H^{[m]},\delta_r^{[m]})\in\boldsymbol{W}(\boldsymbol{0})\times Z\times\boldsymbol{Y}(\boldsymbol{0})\times X$ such that

$$\mathcal{C}_{vv}(\boldsymbol{v}^\delta,\boldsymbol{\delta}_v^{[m]})+\mathcal{C}_{v\hat{p}}(\boldsymbol{v}^\delta,\delta_{\hat{p}}^{[m]})+\mathcal{C}_{vH}(\boldsymbol{v}^\delta,\boldsymbol{\delta}_H^{[m]}) = -\mathcal{R}_v(\boldsymbol{v}^\delta;\boldsymbol{v}^{[m]},\hat{p}^{[m]},\boldsymbol{H}^{[m]}), \quad (17a)$$

$$\mathcal{C}_{\hat{p}v}(\hat{p}^\delta,\boldsymbol{\delta}_v^{[m]}) = -\mathcal{R}_{\hat{p}}(\hat{p}^\delta;\boldsymbol{v}^{[m]}), \quad (17b)$$

$$\mathcal{C}_{HH}(\boldsymbol{H}^\delta,\boldsymbol{\delta}_H^{[m]})+\mathcal{C}_{Hv}(\boldsymbol{H}^\delta,\boldsymbol{\delta}_v^{[m]})+\mathcal{C}_{Hr}(\boldsymbol{H}^\delta,\boldsymbol{\delta}_r^{[m]}) = -\mathcal{R}_H(\boldsymbol{H}^\delta;\boldsymbol{v}^{[m]},\boldsymbol{H}^{[m]},r^{[m]}), \quad (17c)$$

$$\mathcal{C}_{rH}(r^\delta,\boldsymbol{\delta}_H^{[m]}) = -\mathcal{R}_r(r^\delta;\boldsymbol{H}^{[m]}). \quad (17d)$$

for all $(\boldsymbol{v}^\delta,\hat{p}^\delta,\boldsymbol{H}^\delta,r^\delta)\in\boldsymbol{W}(\boldsymbol{0})\times Z\times\boldsymbol{Y}(\boldsymbol{0})\times X$ with $(\boldsymbol{v}^{[0]},\hat{p}^{[0]},\boldsymbol{H}^{[0]},r^{[0]})\in\boldsymbol{W}(\boldsymbol{v}_D)\times Z\times\boldsymbol{Y}(\boldsymbol{f}_D)\times X$.

Note that, by neglecting terms with an underline in (16) the simplified Picard iterative scheme can be obtained [36]. This scheme is fully symmetric with $\mathcal{C}_{vH}(\boldsymbol{v}^\delta,\boldsymbol{\delta}_H^{[m]})=\mathcal{C}_{Hv}(\boldsymbol{\delta}_v^{[m]},\boldsymbol{H}^\delta)$, in addition to the already symmetric terms $\mathcal{C}_{v\hat{p}}(\boldsymbol{v}^\delta,\delta_{\hat{p}}^{[m]})=\mathcal{C}_{\hat{p}v}(\delta_{\hat{p}}^{[m]},\boldsymbol{v}^\delta)$ and $\mathcal{C}_{Hr}(\boldsymbol{H}^\delta,\boldsymbol{\delta}_r^{[m]})=\mathcal{C}_{rH}(\boldsymbol{\delta}_r^{[m]},\boldsymbol{H}^\delta)$. The Newton–Raphson scheme for a homogeneous fluid can be summarised as shown in Algorithm 1.

Algorithm 1. Newton–Raphson scheme for a homogeneous isotropic conducting fluid.

Require: $\boldsymbol{v}^{[m]},\hat{p}^{[m]},\boldsymbol{H}^{[m]},r^{[m]},\mathcal{R}_v^{[m-1]},\mathcal{R}_{\hat{p}}^{[m-1]},\mathcal{R}_H^{[m-1]},\mathcal{R}_r^{[m-1]}$ for $m=0$ and *TOL*

1: **while** $\|\mathcal{R}_v^{[m-1]}\|,\|\mathcal{R}_{\hat{p}}^{[m-1]}\|,\|\mathcal{R}_H^{[m-1]}\|$ and $\|\mathcal{R}_r^{[m-1]}\|\geqslant TOL$ **do**

2: Solve the linear system of Eq. (17) $\rightarrow\boldsymbol{\delta}_v^{[m]},\delta_{\hat{p}}^{[m]},\boldsymbol{\delta}_H^{[m]},\delta_r^{[m]}$

3: Record the residual for step $m\rightarrow\mathcal{R}_v^{[m]},\mathcal{R}_{\hat{p}}^{[m]},\mathcal{R}_H^{[m]}$ and $\mathcal{R}_r^{[m]}$

4: Update the solution with Eq. (15) $\rightarrow\boldsymbol{v}^{[m+1]},\hat{p}^{[m+1]},\boldsymbol{H}^{[m+1]},r^{[m+1]}$

5: $m\leftarrow m+1$

6: **end while**

7: **return** $\boldsymbol{v}\leftarrow\boldsymbol{v}^{[m+1]},\hat{p}\leftarrow\hat{p}^{[m+1]},\boldsymbol{H}\leftarrow\boldsymbol{H}^{[m+1]},r\leftarrow r^{[m+1]}$

3.2. MHD for magenostrictive conducting fluids

In this section we consider the extension of Section 3.1 to more complex magnetostrictive fluids. In order to achieve this we follow Section 2.2 and our own presentation in [26]. In this case, associated with (7), we define for the weak solutions $(\boldsymbol{v},\hat{p},\boldsymbol{H},r)\in\boldsymbol{W}(\boldsymbol{v}_D)\times Z\times\boldsymbol{Y}(\boldsymbol{f}_D)\times X$ the associated residuals $\tilde{\mathcal{R}}_v,\tilde{\mathcal{R}}_{\hat{p}},\tilde{\mathcal{R}}_H$ and $\tilde{\mathcal{R}}_r$ as

$$\tilde{\mathcal{R}}_v(\boldsymbol{v}^\delta;\boldsymbol{v},\hat{p},\boldsymbol{H}) := \int_\Omega \rho(\nabla\boldsymbol{v})\boldsymbol{v}\cdot\boldsymbol{v}^\delta\,\mathrm{d}\Omega+\int_\Omega[[\sigma_F+\sigma_{EM}]] : [[\varepsilon(\boldsymbol{v}^\delta)]]\mathrm{d}\Omega-\int_\Omega\tilde{\boldsymbol{f}}\cdot\boldsymbol{v}^\delta\,\mathrm{d}\Omega-\int_{\partial\Omega_N^F}\boldsymbol{t}\cdot\boldsymbol{v}^\delta\,\mathrm{d}\partial\Omega, \quad (18a)$$

$$\tilde{\mathcal{R}}_{\hat{p}}(\hat{p}^\delta;\boldsymbol{v}) := \int_\Omega(\nabla\cdot\boldsymbol{v})\hat{p}^\delta\,\mathrm{d}\Omega, \quad (18b)$$

$$\tilde{\mathcal{R}}_H(\boldsymbol{H}^\delta;\boldsymbol{v},\boldsymbol{H},r) := -\int_\Omega c[[\tilde{\sigma}]]^{-1}\nabla\times\boldsymbol{H}\cdot\nabla\times\boldsymbol{H}^\delta\,\mathrm{d}\Omega + \int_\Omega\boldsymbol{v}\times([[\mu_r(\boldsymbol{v})]]\boldsymbol{H})\cdot\nabla\times\boldsymbol{H}^\delta\,\mathrm{d}\Omega - \int_\Omega([[\mu_r(\boldsymbol{v})]]\nabla r)\cdot\boldsymbol{H}^\delta\,\mathrm{d}\Omega+\int_\Omega\boldsymbol{g}\cdot\boldsymbol{H}^\delta\,\mathrm{d}\Omega - \int_{\partial\Omega_N^M}\boldsymbol{f}_N\cdot\boldsymbol{H}^\delta\,\mathrm{d}\partial\Omega, \quad (18c)$$

$$\tilde{\mathcal{R}}_r(r^\delta;\boldsymbol{H},\boldsymbol{v}) := -\int_\Omega([[\mu_r(\boldsymbol{v})]]\boldsymbol{H})\cdot\nabla r^\delta\,\mathrm{d}\Omega, \quad (18d)$$

for all $(\boldsymbol{v}^\delta,\hat{p}^\delta,\boldsymbol{H}^\delta,r^\delta)\in\boldsymbol{W}(\boldsymbol{0})\times Z\times\boldsymbol{Y}(\boldsymbol{0})\times X$. Note that in the case of non-pure Dirichlet conditions the constraint of $\int_\Omega\hat{p}\,\mathrm{d}\Omega=0$ in Z can also be dropped.

Analogue to the previous section, with the possible trial solutions $(\boldsymbol{v}^{[m]},\hat{p}^{[m]},\boldsymbol{H}^{[m]},r^{[m]})\in\tilde{\boldsymbol{W}}(\boldsymbol{v}_D)\times Z\times\tilde{\boldsymbol{Y}}(\boldsymbol{f}_D)\times X$, the linearised residuals (18) can be written as follows

$$\tilde{\mathcal{R}}_v(\boldsymbol{v}^\delta;\boldsymbol{v}^{[m]},\hat{p}^{[m]},\boldsymbol{H}^{[m]})+\mathcal{D}\tilde{\mathcal{R}}_v(\boldsymbol{v}^\delta;\boldsymbol{v}^{[m]},\hat{p}^{[m]},\boldsymbol{H}^{[m]})[\boldsymbol{\delta}_v^{[m]}] +\mathcal{D}\tilde{\mathcal{R}}_v(\boldsymbol{v}^\delta;\boldsymbol{v}^{[m]},\hat{p}^{[m]},\boldsymbol{H}^{[m]})[\boldsymbol{\delta}_{\hat{p}}^{[m]}]+\mathcal{D}\tilde{\mathcal{R}}_v(\boldsymbol{v}^\delta;\boldsymbol{v}^{[m]},\hat{p}^{[m]},\boldsymbol{H}^{[m]})[\boldsymbol{\delta}_H^{[m]}]=0, \quad (19a)$$

$$\tilde{\mathcal{R}}_{\hat{p}}(\hat{p}^\delta;\boldsymbol{v}^{[m]})+\mathcal{D}\tilde{\mathcal{R}}_{\hat{p}}(\hat{p}^\delta;\boldsymbol{v}^{[m]}[\boldsymbol{\delta}_v^{[m]}]=0, \quad (19b)$$

$$\tilde{\mathcal{R}}_H(\boldsymbol{H}^\delta;\boldsymbol{v}^{[m]},\boldsymbol{H}^{[m]},r^{[m]})+\mathcal{D}\tilde{\mathcal{R}}_H(\boldsymbol{H}^\delta;\boldsymbol{v}^{[m]},\boldsymbol{H}^{[m]},r^{[m]})[\boldsymbol{\delta}_H^{[m]}] +\mathcal{D}\tilde{\mathcal{R}}_H(\boldsymbol{H}^\delta;\boldsymbol{v}^{[m]},\boldsymbol{H}^{[m]},r^{[m]})[\boldsymbol{\delta}_v^{[m]}]+\mathcal{D}\tilde{\mathcal{R}}_H(\boldsymbol{H}^\delta;\boldsymbol{v}^{[m]},\boldsymbol{H}^{[m]},r^{[m]})[\boldsymbol{\delta}_r^{[m]}]=0, \quad (19c)$$

$$\tilde{\mathcal{R}}_r(r^\delta;\boldsymbol{v}^{[m]},\boldsymbol{H}^{[m]})+\mathcal{D}\tilde{\mathcal{R}}_r(r^\delta;\boldsymbol{v}^{[m]},\boldsymbol{H}^{[m]})[\boldsymbol{\delta}_v^{[m]}]+\mathcal{D}\tilde{\mathcal{R}}_r(r^\delta;\boldsymbol{v}^{[m]},\boldsymbol{H}^{[m]})[\boldsymbol{\delta}_H^{[m]}]=0, \quad (19d)$$

for all $(\boldsymbol{v}^\delta,\hat{p}^\delta,\boldsymbol{H}^\delta,r^\delta)\in\tilde{\boldsymbol{W}}(\boldsymbol{0})\times Z\times\tilde{\boldsymbol{Y}}(\boldsymbol{0})\times X$ with similar update equations to (15).

The directional derivatives are

$$\mathcal{D}\tilde{\mathcal{R}}_v(\boldsymbol{v}^\delta;\boldsymbol{v}^{[m]},\hat{p}^{[m]},\boldsymbol{H}^{[m]})[\boldsymbol{\delta}_v^{[m]}]=\mathcal{DR}_v(\boldsymbol{v}^\delta;\boldsymbol{v}^{[m]},\hat{p}^{[m]},\boldsymbol{H}^{[m]})[\boldsymbol{\delta}_v^{[m]}], \quad (20a)$$

$$\mathcal{D}\tilde{\mathcal{R}}_v(\boldsymbol{v}^\delta;\boldsymbol{v}^{[m]},\hat{p}^{[m]},\boldsymbol{H}^{[m]})[\boldsymbol{\delta}_{\hat{p}}^{[m]}]=\mathcal{DR}_v(\boldsymbol{v}^\delta;\boldsymbol{v}^{[m]},\hat{p}^{[m]},\boldsymbol{H}^{[m]})[\boldsymbol{\delta}_{\hat{p}}^{[m]}], \quad (20b)$$

$$\mathcal{D}\tilde{\mathcal{R}}_v(\boldsymbol{v}^\delta;\boldsymbol{v}^{[m]},\hat{p}^{[m]},\boldsymbol{H}^{[m]})[\boldsymbol{\delta}_H^{[m]}]=\int_\Omega[[\varepsilon(\boldsymbol{v}^\delta)]]:\frac{\partial[[\sigma_{EM}]]}{\partial\boldsymbol{H}}\boldsymbol{\delta}_H^{[m]}\,\mathrm{d}\Omega, \quad (20c)$$

$$\mathcal{D}\tilde{\mathcal{R}}_{\hat{p}}(\hat{p}^\delta;\boldsymbol{v}^{[m]})[\boldsymbol{\delta}_v^{[m]}]=\mathcal{DR}_{\hat{p}}(\hat{p}^\delta;\boldsymbol{v}^{[m]})[\boldsymbol{\delta}_v^{[m]}], \quad (20d)$$

$$\mathcal{D}\tilde{\mathcal{R}}_H(\boldsymbol{H}^\delta;\boldsymbol{v}^{[m]},\boldsymbol{H}^{[m]},r^{[m]})[\delta_H^{[m]}] = -\int_\Omega c[[\tilde{\sigma}]]^{-1}\nabla\times\boldsymbol{\delta}_H^{[m]}\cdot\nabla\times\boldsymbol{H}^\delta\,\mathrm{d}\Omega + \int_\Omega \boldsymbol{v}^{[m]}\times([[\mu_r(\boldsymbol{v}^{[m]})]]\delta_H^{[m]})\cdot\nabla\times\boldsymbol{H}^\delta\,\mathrm{d}\Omega, \tag{20e}$$

$$\mathcal{D}\tilde{\mathcal{R}}_H(\boldsymbol{H}^\delta;\boldsymbol{v}^{[m]},\boldsymbol{H}^{[m]},r^{[m]})[\delta_v^{[m]}] = \int_\Omega(\boldsymbol{\delta}_v^{[m]}\times[[\mu_r(\boldsymbol{v}^{[m]})]]\boldsymbol{H}^{[m]})\cdot\nabla\times\boldsymbol{H}^\delta\,\mathrm{d}\Omega + \int_\Omega \boldsymbol{v}^{[m]}\times\left(\frac{\partial([[\mu_r]]\boldsymbol{H})}{\partial[[\varepsilon]]}:[[\varepsilon(\boldsymbol{\delta}_v^{[m]})]]\right)\cdot\nabla\times\boldsymbol{H}^\delta\,\mathrm{d}\Omega, \tag{20f}$$

$$\mathcal{D}\tilde{\mathcal{R}}_H(\boldsymbol{H}^\delta;\boldsymbol{v}^{[m]},\boldsymbol{H}^{[m]},r^{[m]})[\delta_r^{[m]}] = -\int_\Omega[[\mu_r(\boldsymbol{v}^{[m]})]]\nabla\delta_r^{[m]}\cdot\boldsymbol{H}^\delta\,\mathrm{d}\Omega, \tag{20g}$$

$$\mathcal{D}\tilde{\mathcal{R}}_r(r^\delta;\boldsymbol{v}^{[m]},\boldsymbol{H}^{[m]})[\boldsymbol{\delta}_v^{[m]}] = -\int_\Omega\nabla r^\delta\cdot\frac{\partial([[\mu_r]]\boldsymbol{H})}{\partial[[\varepsilon]]}:[[\varepsilon(\boldsymbol{\delta}_v^{[m]})]]\,\mathrm{d}\Omega, \tag{20h}$$

$$\mathcal{D}\tilde{\mathcal{R}}_r(r^\delta;\boldsymbol{v}^{[m]},\boldsymbol{H}^{[m]})[\boldsymbol{\delta}_H^{[m]}] = -\int_\Omega[[\mu_r(\boldsymbol{v}^{[m]})]]\boldsymbol{\delta}_H^{[m]}\cdot\nabla r^\delta\,\mathrm{d}\Omega. \tag{20i}$$

In the above

$$\left[\frac{\partial[[\sigma_{EM}]]}{\partial\boldsymbol{H}}\right]_{ijk} = \left(\mu_r-\frac{\mu_r^{(1)}}{2}\right)(\delta_{ik}H_j+\delta_{jk}H_i)-(\mu_r+\mu_r^{(2)})\delta_{ij}H_k,$$

$$\left[\frac{\partial([[\mu]]\boldsymbol{H})}{\partial[[\varepsilon]]}\right]_{ijk} = (\mu_r+\mu_r^{(2)})\delta_{jk}H_i+(\mu_r^{(1)}-2\mu_r)\delta_{ij}H_k.$$

Assuming the solutions $(\boldsymbol{v}^{[m]},\hat{p}^{[m]},\boldsymbol{H}^{[m]},r^{[m]})$ to be known, and associating the bilinear forms $\tilde{\mathcal{C}}_{vH}$, $\tilde{\mathcal{C}}_{HH},\tilde{\mathcal{C}}_{Hv},\tilde{\mathcal{C}}_{Hr},\tilde{\mathcal{C}}_{rv}$ and $\tilde{\mathcal{C}}_{rH}$ in turn with the new directional derivatives stated above, the Newton–Raphson iteration can be stated as: Find $(\boldsymbol{\delta}_v^{[m]},\delta_{\hat{p}}^{[m]},\boldsymbol{\delta}_H^{[m]},\delta_r^{[m]})\in\boldsymbol{W}(\boldsymbol{0})\times Z\times\boldsymbol{Y}(\boldsymbol{0})\times X$ such that

$$\mathcal{C}_{vv}(\boldsymbol{v}^\delta,\boldsymbol{\delta}_v^{[m]})+\mathcal{C}_{v\hat{p}}(\boldsymbol{v}^\delta,\delta_{\hat{p}}^{[m]})+\tilde{\mathcal{C}}_{vH}(\boldsymbol{v}^\delta,\boldsymbol{\delta}_H^{[m]}) = -\tilde{\mathcal{R}}_v(\boldsymbol{v}^\delta;\boldsymbol{v}^{[m]},\hat{p}^{[m]},\boldsymbol{H}^{[m]}), \tag{21a}$$

$$\mathcal{C}_{\hat{p}v}(\hat{p}^\delta,\boldsymbol{\delta}_v^{[m]}]) = -\tilde{\mathcal{R}}_{\hat{p}}(\hat{p}^\delta;\boldsymbol{v}^{[m]}), \tag{21b}$$

$$\tilde{\mathcal{C}}_{HH}(\boldsymbol{H}^\delta,\boldsymbol{\delta}_H^{[m]})+\tilde{\mathcal{C}}_{Hv}(\boldsymbol{H}^\delta,\boldsymbol{\delta}_v^{[m]})+\tilde{\mathcal{C}}_{Hr}(\boldsymbol{H}^\delta,\boldsymbol{\delta}_r^{[m]}) = -\tilde{\mathcal{R}}_H(\boldsymbol{H}^\delta;\boldsymbol{v}^{[m]},\boldsymbol{H}^{[m]},r^{[m]}), \tag{21c}$$

$$\tilde{\mathcal{C}}_{rv}(r^\delta,\boldsymbol{\delta}_v^{[m]})+\tilde{\mathcal{C}}_{r\boldsymbol{H}}(r^\delta,\boldsymbol{\delta}_H^{[m]}) = -\tilde{\mathcal{R}}_r(r^\delta;\boldsymbol{H}^{[m]}). \tag{21d}$$

for all $(\boldsymbol{v}^\delta,\hat{p}^\delta,\boldsymbol{H}^\delta,r^\delta)\in\boldsymbol{W}(\boldsymbol{0})\times Z\times\boldsymbol{Y}(\boldsymbol{0})\times X$ with $(\boldsymbol{v}^{[0]},\hat{p}^{[0]},\boldsymbol{H}^{[0]},r^{[0]})\in\boldsymbol{W}(\boldsymbol{v}_D)\times Z\times\boldsymbol{Y}(\boldsymbol{f}_D)\times X$. Note that this reduces to (17) for a homogeneous isotropic conducting fluid without magnetostrictive effects. The Newton–Raphson scheme for a magnetostrictive material can be summarised as shown in Algorithm 2.

Algorithm 2. Newton–Raphson scheme for a magnetostrictive fluid.

Require: $\boldsymbol{v}^{[m]},\hat{p}^{[m]},\boldsymbol{H}^{[m]},r^{[m]},\tilde{\mathcal{R}}_v^{[m-1]},\tilde{\mathcal{R}}_{\hat{p}}^{[m-1]},\tilde{\mathcal{R}}_H^{[m-1]},\tilde{\mathcal{R}}_r^{[m-1]}$ for $m=0$ and *TOL*

while $\|\tilde{\mathcal{R}}_v^{[m-1]}\|,\|\tilde{\mathcal{R}}_{\hat{p}}^{[m-1]}\|,\|\tilde{\mathcal{R}}_H^{[m-1]}\|$ and $\|\tilde{\mathcal{R}}_r^{[m-1]}\|\geqslant TOL$ **do**

  Solve the linear system of Eq. (21) $\rightarrow\delta_v^{[m]},\delta_{\hat{p}}^{[m]},\delta_H^{[m]},\delta_r^{[m]}$

  Record the residual for step $m\rightarrow\tilde{\mathcal{R}}_v^{[m]},\tilde{\mathcal{R}}_{\hat{p}}^{[m]},\tilde{\mathcal{R}}_H^{[m]}$ and $\tilde{\mathcal{R}}_r^{[m]}$

  Update the solution with Eq. (15) $\rightarrow\boldsymbol{v}^{[m+1]},\hat{p}^{[m+1]},\boldsymbol{H}^{[m+1]},r^{[m+1]}$

  $m\leftarrow m+1$

end while

return $\boldsymbol{v}\leftarrow\boldsymbol{v}^{[m+1]},\hat{p}\leftarrow\hat{p}^{[m+1]},\boldsymbol{H}\leftarrow\boldsymbol{H}^{[m+1]},r\leftarrow r^{[m+1]}$

4. *hp*-Discretisation

The *hp*-finite element discretisation of (17) and (21) follows similar lines to that already discussed in [17,26], where we employ the *hp*-finite element discretisation of Schöberl and Zaglmayr [35,40]. In the following, we discuss the discretisation for an unstructured tetrahedral discretisation for $d=3$, the corresponding triangular discretisation for $d=2$ follows mostly by obvious simplifications. For this we consider a regular simplicial triangulation of Ω denoted by $\mathcal{T}_h$, with the set of vertices $\mathcal{V}_h$, the set of edges $\mathcal{E}_h$ and the set of faces $\mathcal{F}_h$ and recall the low-order vertex, high-order edge-face-cell based splitting of the hierarchic scalar H^1 conforming finite element space

$$X_{h,p} := X_{h,1}\oplus\sum_{\text{edges }E\in\mathcal{E}_h}X_p^E\oplus\sum_{\text{faces }F\in\mathcal{F}_h}X_p^F\oplus\sum_{\text{cells }I\in\mathcal{T}_h}X_p^I\subset H^1(\Omega),$$

where $X_{h,1}$ is the classical space of continuous piecewise linear hat functions and X_p^E,X_p^F,X_p^I denote its hierarchic edge, face and cell enrichment. In the case of a uniform polynomial degree we obtain the space of polynomials of total degree p, i.e. $X_{h,p}|_T := P^p(T)$ on each element $T\in\mathcal{T}_h$ employed. For problems in this work we require a discretisation of the vector $\boldsymbol{H}(\mathrm{curl})$ conforming space, employing the approach of Schöberl and Zaglmayr [35,40] this results in the splitting low order edge, high order edge-face-cell based splitting

$$\boldsymbol{Y}_{h,p} := \boldsymbol{Y}_{h,0}\oplus\sum_{\text{edges }E\in\mathcal{E}_h}\boldsymbol{Y}_p^E\oplus\sum_{\text{faces }F\in\mathcal{F}_h}\boldsymbol{Y}_p^F\oplus\sum_{\text{cells }I\in\mathcal{T}_h}\boldsymbol{Y}_p^I\subset\boldsymbol{H}(\mathrm{curl},\Omega),$$

where $\boldsymbol{Y}_{h,0}$ is the classical Nédélec element with continuous constant tangential components on edges and $\boldsymbol{Y}_p^E,\boldsymbol{Y}_p^F,\boldsymbol{Y}_p^I$ denote its hierarchic edge, face and cell enrichment. In addition, we set

$$\boldsymbol{W}_{h,p} := \{\boldsymbol{v}:\boldsymbol{v}\in(X_{h,p})^3\},$$

$$Z_{h,p-1} := Z_{h,0}\oplus\sum_{\text{cells }I\in\mathcal{T}_h}Z_{p-1}^I\subset L_2(\Omega),$$

where $Z_{h,0}$ is the space of classical scalar finite element space of piecewise constants. We present below the fully discretised version of (17), which must be solved at each Newton–Raphson iteration for

a simple conducting fluid. Then, in Section 4.2, we present the corresponding discretised version of (21) for the case of a conducting magnetostrictive fluid.

4.1. Homogeneous isotropic conducting fluids

The mth step of the discrete Newton–Raphson scheme for this fluid in $d=3$ is: Find $(\boldsymbol{\delta}^{[m]}_{v,hp}, \delta^{[m]}_{\hat{p},hp}, \boldsymbol{\delta}^{[m]}_{H,hp}, \delta^{[m]}_{r,hp}) \in \boldsymbol{W}(\boldsymbol{0}) \cap \boldsymbol{W}_{hp+2} \times Z \cap Z_{hp-1} \times \boldsymbol{Y}(\boldsymbol{0}) \cap \boldsymbol{Y}_{hp+1} \times X \cap X_{hp+2}$ such that

$$\mathcal{C}_{vv}(\boldsymbol{v}^{\delta}_{hp}, \boldsymbol{\delta}^{[m]}_{v,hp}) + \mathcal{C}_{v\hat{p}}(\boldsymbol{v}^{\delta}_{hp}, \delta^{[m]}_{\hat{p},hp}) + \mathcal{C}_{vH}(\boldsymbol{v}^{\delta}_{hp}, \boldsymbol{\delta}^{[m]}_{H,hp}) = -\mathcal{R}_{v}(\boldsymbol{v}^{\delta}_{hp}; \boldsymbol{v}^{[m]}_{hp}, \hat{p}^{[m]}_{hp}, \boldsymbol{H}^{[m]}_{hp}), \tag{22a}$$

$$\mathcal{C}_{\hat{p}v}(\hat{p}^{\delta}_{hp}, \boldsymbol{\delta}^{[m]}_{v,hp}) = -\mathcal{R}_{\hat{p}}(\hat{p}^{\delta}_{hp}; \boldsymbol{v}^{[m]}_{hp}), \tag{22b}$$

$$\mathcal{C}_{HH}(\boldsymbol{H}^{\delta}_{hp}, \boldsymbol{\delta}^{[m]}_{H,hp}) + \mathcal{C}_{Hv}(\boldsymbol{H}^{\delta}_{hp}, \boldsymbol{\delta}^{[m]}_{v,hp}) + \mathcal{C}_{Hr}(\boldsymbol{H}^{\delta}_{hp}, \boldsymbol{\delta}^{[m]}_{r,hp}) = -\mathcal{R}_{H}(\boldsymbol{H}^{\delta}_{hp}; \boldsymbol{v}^{[m]}_{hp}, \boldsymbol{H}^{[m]}_{hp}, r^{[m]}_{hp}), \tag{22c}$$

$$\mathcal{C}_{rH}(r^{\delta}_{hp}, \boldsymbol{\delta}^{[m]}_{H,hp}) = -\mathcal{R}_{r}(r^{\delta}_{hp}; \boldsymbol{H}^{[m]}_{hp}). \tag{22d}$$

for all $(\boldsymbol{v}^{\delta}_{hp}, \hat{p}^{\delta}_{hp}, \boldsymbol{H}^{\delta}_{hp}, r^{\delta}_{hp}) \in \boldsymbol{W}(\boldsymbol{0}) \cap \boldsymbol{W}_{hp+2} \times Z \cap Z_{hp-1} \times \boldsymbol{Y}(\boldsymbol{0}) \cap \boldsymbol{Y}_{hp+1} \times X \cap X_{hp+2}$. The update equations are similar to those given in (15). It is important to note the need to use different sets of basis functions for the different fields but, also, the need to use different polynomial degrees. For $d=2$ triangular elements, the updates of velocity $\boldsymbol{\delta}^{[m]}_{v,hp}$ and pressure $\delta^{[m]}_{\hat{p},hp}$ are approximated as polynomials of degree P_p, P_{p-2} in order to satisfy the LBB condition [37]. For $d=3$, the updates of velocity $\boldsymbol{\delta}^{[m]}_{v,hp}$ and pressure $\delta^{[m]}_{\hat{p},hp}$ are approximated as polynomials of degree P_p, P_{p-3} in order to satisfy the LBB condition for tetrahedral elements for this case [8,37]. The updates of the magnetic field $\boldsymbol{\delta}^{[m]}_{H,hp}$ and the Lagrange multiplier $\delta^{[m]}_{r,hp}$ are selected to be P_{p-1}, P_p for both $d=2$ and $d=3$ [8].

4.2. Conducting magnetostrictive fluids

The mth step of the discrete Newton–Raphson scheme for a conducting fluid including magnetostrictive effects in $d=3$ is: Find $(\boldsymbol{\delta}^{[m]}_{v,hp}, \delta^{[m]}_{\hat{p},hp}, \boldsymbol{\delta}^{[m]}_{H,hp}, \delta^{[m]}_{r,hp}) \in \boldsymbol{W}(\boldsymbol{0}) \cap \boldsymbol{W}_{hp+2} \times Z \cap Z_{hp-1} \times \boldsymbol{Y}(\boldsymbol{0}) \cap \boldsymbol{Y}_{hp+1} \times X \cap X_{hp+2}$ such that

$$\mathcal{C}_{vv}(\boldsymbol{v}^{\delta}_{hp}, \boldsymbol{\delta}^{[m]}_{v,hp}) + \mathcal{C}_{v\hat{p}}(\boldsymbol{v}^{\delta}_{hp}, \delta^{[m]}_{\hat{p},hp}) + \tilde{\mathcal{C}}_{vH}(\boldsymbol{v}^{\delta}_{hp}, \boldsymbol{\delta}^{[m]}_{H,hp}) = -\tilde{\mathcal{R}}_{v}(\boldsymbol{v}^{\delta}_{hp}; \boldsymbol{v}^{[m]}_{hp}, \hat{p}^{[m]}_{hp}, \boldsymbol{H}^{[m]}_{hp}), \tag{23a}$$

$$\mathcal{C}_{\hat{p}v}(\hat{p}^{\delta}_{hp}, \boldsymbol{\delta}^{[m]}_{v,hp}]) = -\tilde{\mathcal{R}}_{\hat{p}}(\hat{p}^{\delta}_{hp}; \boldsymbol{v}^{[m]}_{hp}), \tag{23b}$$

$$\tilde{\mathcal{C}}_{HH}(\boldsymbol{H}^{\delta}_{hp}, \boldsymbol{\delta}^{[m]}_{H,hp}) + \tilde{\mathcal{C}}_{Hv}(\boldsymbol{H}^{\delta}_{hp}, \boldsymbol{\delta}^{[m]}_{v,hp}) + \tilde{\mathcal{C}}_{Hr}(\boldsymbol{H}^{\delta}_{hp}, \boldsymbol{\delta}^{[m]}_{r}) = -\tilde{\mathcal{R}}_{H}(\boldsymbol{H}^{\delta}_{hp}; \boldsymbol{v}^{[m]}_{hp}, \boldsymbol{H}^{[m]}_{hp}, r^{[m]}_{hp}), \tag{23c}$$

$$\tilde{\mathcal{C}}_{rv}(r^{\delta}_{hp}, \boldsymbol{\delta}^{[m]}_{v,hp}) + \tilde{\mathcal{C}}_{r\boldsymbol{H}}(r^{\delta}_{hp}, \boldsymbol{\delta}^{[m]}_{H,hp}) = -\tilde{\mathcal{R}}_{r}(r^{\delta}; \boldsymbol{H}^{[m]}), \tag{23d}$$

for all $(\boldsymbol{v}^{\delta}_{hp}, \hat{p}^{\delta}_{hp}, \boldsymbol{H}^{\delta}_{hp}, r^{\delta}_{hp}) \in \boldsymbol{W}(\boldsymbol{0}) \cap \boldsymbol{W}_{hp+2} \times Z \cap Z_{hp-1} \times \boldsymbol{Y}(\boldsymbol{0}) \cap \boldsymbol{Y}_{hp+1} \times X \cap X_{hp+2}$. In the above, terms with a tilde are different from those in (22), which have been constructed in order to include magntostrictive effects, but do reduce to their previous forms in the case of a homogeneous isotropic conducting fluid. The polynomial orders are taken as described in Section 4.1.

5. Numerical examples

A series of numerical examples are presented to benchmark our approach by applying it to the simulation of MHD problems in $d=2,3$ with known analytical solutions. Then, the predictive capability of our approach is considered by applying it to the simulation of problems in $d=2,3$, which include non-homogeneous media and magnetostrictive effects, that do not have analytical solutions.

5.1. Two-dimensional problems

In order to verify the $d=2$ implementation, we apply the scheme to several well-known benchmarking problems. We start from a simplified linearised case with smooth and singular solutions. We then progress to the fully coupled problem, where a smooth problem and the well known Hartmann flow problem [18,9,15] are used for verification.

5.1.1. Linearised L-shape domain smooth problem

The first example consists of an L-shaped domain $\Omega = (-1,1)^2 \setminus ([0,1) \times (-1,0])$ on which we consider the solution of a linearised MHD problem [36] by considering $[[\mu_r]] = c[[\tilde{\sigma}]]^{-1} = [[\mathbb{I}]]$ and $\rho = \hat{\mu} = 1$. For this linearised problem, only a single step of the Picard iteration scheme is required for which we set

$$\boldsymbol{v}^{[0]} = \begin{pmatrix} 2 \\ 1 \end{pmatrix}, \quad \boldsymbol{H}^{[0]} = \begin{pmatrix} x \\ -y \end{pmatrix} \quad \text{in } \Omega,$$

and choose $\tilde{\boldsymbol{f}}$ and $\boldsymbol{g}$ so that the analytical solution is [23]

$$\boldsymbol{\delta}_v = \begin{pmatrix} -(y\cos y + \sin y)e^x \\ y \sin y e^x \end{pmatrix}, \quad \delta_{\hat{p}} = 2e^x \sin y, \qquad \boldsymbol{\delta}_H = \begin{pmatrix} -(y\cos y + \sin y)e^x \\ y \sin y e^x \end{pmatrix}, \quad \delta_r = -\sin \pi x \ \sin \pi y, \tag{24}$$

in Ω. Then, the boundary conditions are different to those in Algorithm 1 and are of the form $\boldsymbol{\delta}^{[0]}_{v,hp} = \boldsymbol{\delta}_v$ on $\partial\Omega^F_D = \partial\Omega$ and $\boldsymbol{n} \times \boldsymbol{\delta}^{[0]}_{H,hp} = \boldsymbol{n} \times \boldsymbol{\delta}_H$ on $\partial\Omega^M_D = \partial\Omega$. As the analytical solution is smooth, we consider a fixed uniform mesh consisting of 382 triangular elements and apply uniform p-refinement with polynomial degrees $p = 2,3,4,5,6$, where p refers to the degree of the H^1 conforming approximation and the degrees of the approximation for the other variables are chosen to satisfy the LBB constraints (see Section 4.1). Unless otherwise stated, we follow this convention for naming p in each of the following examples.

In Fig. 2(a) we show the convergence of $\|\boldsymbol{\delta}_v - \boldsymbol{\delta}^{[0]}_{v,hp}\|_{H^1}$ and $\|\boldsymbol{\delta}_H - \boldsymbol{\delta}^{[0]}_{H,hp}\|_{\boldsymbol{H}(\mathrm{curl})}$, which both indicate a downward sloping curve confirming the expected exponential convergence of p-refinement for this smooth problem. In Fig. 2(b) we show the computed streamlines for $\boldsymbol{\delta}^{[0]}_{v,hp}$ for the converged solution.

5.1.2. Linearised L-shape domain singular problem

We again consider the L-shaped domain described in the previous subsection for the linearised MHD problem with the same material parameters as described above. Let us consider a single step of the Picard iteration with

$$\boldsymbol{v}^{[0]} = \begin{pmatrix} 0 \\ 0 \end{pmatrix}, \quad \boldsymbol{H}^{[0]} = \begin{pmatrix} -1 \\ 1 \end{pmatrix} \quad \text{in } \Omega,$$

and $\tilde{\boldsymbol{f}}$ and $\boldsymbol{g}$ selected so that the analytical solution is [23]

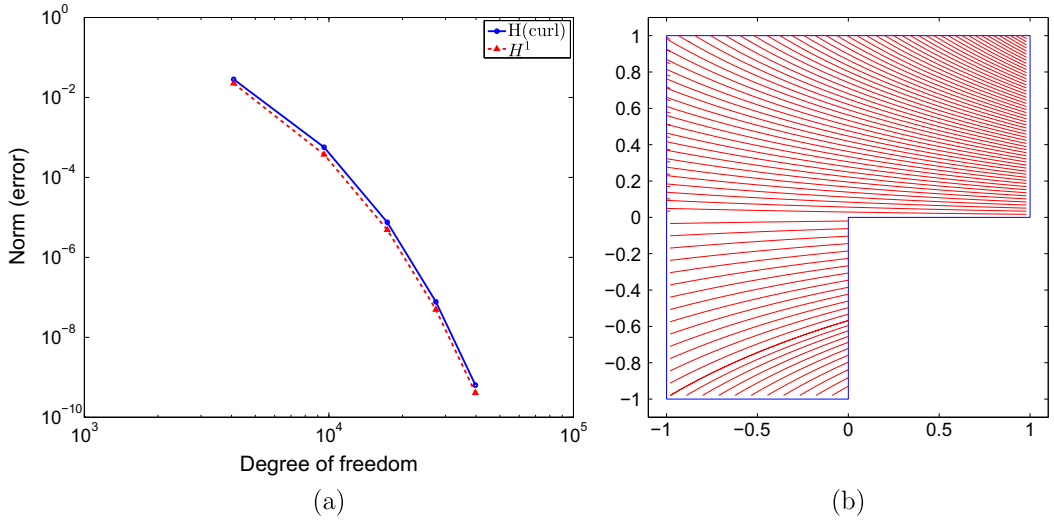

Fig. 2. Two-dimensional L-shape domain with a smooth solution showing: (a) the convergence of $\left\|\boldsymbol{\delta}_v - \boldsymbol{\delta}^{[0]}_{v,hp}\right\|_{H^1}$ and $\left\|\boldsymbol{\delta}_H - \boldsymbol{\delta}^{[0]}_{H,hp}\right\|_{\boldsymbol{H}(\mathrm{curl})}$ with p-refinement and (b) the streamlines $\boldsymbol{\delta}^{[0]}_{v,hp}$.

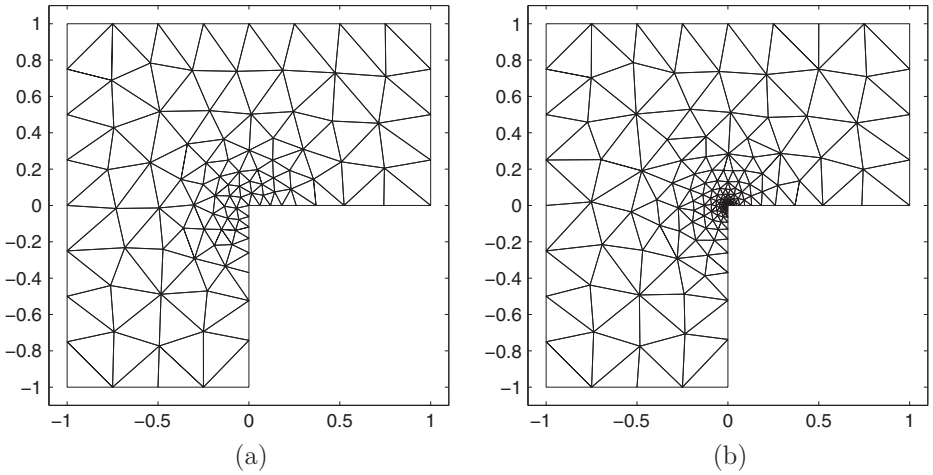

Fig. 3. Two-dimensional L-shape domain with a singularity showing: unstructured graded meshes with (a)176 (grading factor 3) and (b) 308 (grading factor 5) triangular elements, respectively.

$$
\begin{aligned}
\boldsymbol{\delta}_v &= \begin{pmatrix} \hat{\rho}^{\lambda}((1+\lambda)\sin(\phi)\psi(\phi) + \cos(\phi)\psi'(\phi)) \\ \hat{\rho}^{\lambda}(-(1+\lambda)\cos(\phi)\psi(\phi) + \sin(\phi)\psi'(\phi)) \end{pmatrix}, \\
\delta_{\hat{p}} &= -\hat{\rho}^{\lambda-1}((1+\lambda)^2\psi'(\phi) + \psi'''(\phi))/(1-\lambda), \\
\boldsymbol{\delta}_H &= \nabla(\hat{\rho}^{2/3}\sin(2/3\phi)), \\
\delta_r &= 0,
\end{aligned} \tag{25}
$$

in Ω where

$$
\begin{aligned}
\psi(\phi) = {} & \sin((1+\lambda)\phi)\cos(\lambda w)/(1+\lambda) - \cos((1+\lambda)\phi) \\
& - \sin((1-\lambda)\phi)\cos(\lambda w)/(1-\lambda) + \cos((1-\lambda)\phi).
\end{aligned} \tag{26}
$$

In the above $(\hat{\rho}, \phi)$ represent the polar coordinates centred at $x = 0, y = 0$ and, for the case where $\omega = \frac{3}{2}\pi$ and $\lambda \approx 0.54448373678246$, the analytical solution exhibits a strong magnetic singularity at the origin [23]. The boundary conditions are analogous to Section 5.1.1.

A series of meshes are constructed with geometric refinement towards the re-entrant corner (and the location of singularity), the geometric refinement factors are 2, 3, 4, 5 and 6, respectively. Illustrations of typical meshes with grading factors 3 and 6, and 176 and 308 unstructured triangles, respectively, are shown in Fig. 3.

On these meshes we apply uniform p-refinement with polynomial degrees $p = 2, 3, 4, 5, 6$ leading to the results shown in Fig. 4 (a) where the convergence of $\|\boldsymbol{\delta}_v - \boldsymbol{\delta}^{[0]}_{v,hp}\|_{H^1}$ and $\|\boldsymbol{\delta}_H - \boldsymbol{\delta}^{[0]}_{H,hp}\|_{\boldsymbol{H}(\mathrm{curl})}$ can be observed. As expected, a family of convergence curves are produced and each show a similar behaviour: initially p-refinement on particular grid produces a rapid convergence of the error, which then slows to an algebraic rate of convergence with further increments of p. By combining both h- and p-refinements the resulting error envelope is a downward sloping curve, confirming the expected exponential convergence for this problem with a strong singularity. Fig. 4(b) shows the computed streamlines for $\boldsymbol{\delta}^{[0]}_{v,hp}$ for the converged solution. In Fig. 4(c) and (d), the computed contours for the x and y components of $\boldsymbol{\delta}^{[0]}_{H,hp}$, for the converged solution, are presented from which we can observe the strong singularity towards the re-entrant corner.

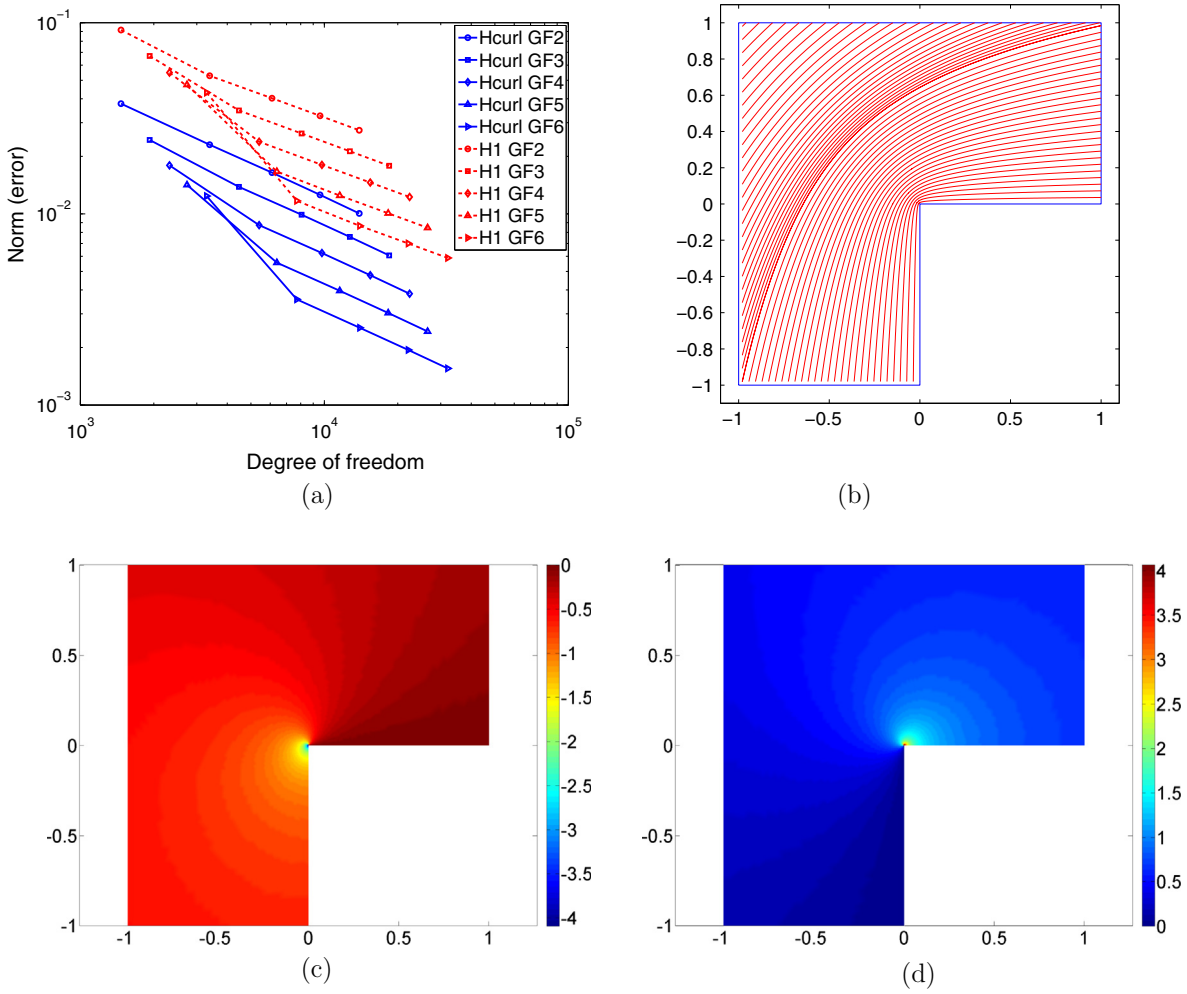

Fig. 4. Two-dimensional L-shaped domain with *i*th a singularity showing: (a) the convergence of $\left\|\boldsymbol{\delta}_v - \boldsymbol{\delta}_{v,hp}^{[0]}\right\|_{H^1}$ and $\left\|\boldsymbol{\delta}_H - \boldsymbol{\delta}_{H,hp}^{[0]}\right\|_{\boldsymbol{H}(\mathrm{curl})}$ with *hp*-refinement, (b) the streamlines $\boldsymbol{\delta}_{v,hp}^{[0]}$ and (c), (d) contours of the *x* and *y* components of $\boldsymbol{\delta}_{H,hp}^{[0]}$.

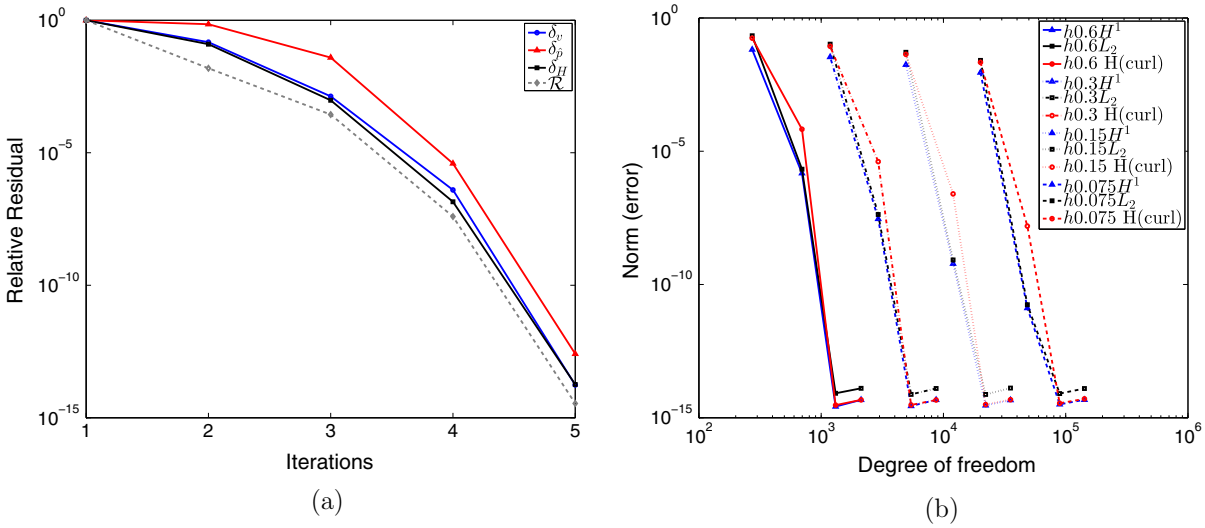

Fig. 5. Two-dimensional square domain with smooth solution showing: (a) the quadratic convergence for updates $\boldsymbol{\delta}_v, \delta_{\hat{p}}, \boldsymbol{\delta}_H$ and the relative residual $\mathcal{R}$ for the Newton–Raphson implementation with uniform $p = 5$ elements and (b) the convergence of $\left\|\boldsymbol{v} - \boldsymbol{v}_{hp}^{[M]}\right\|_{H^1}$, $\left\|\hat{p} - \hat{p}_{hp}^{[M]}\right\|_{L_2}$ and $\left\|\boldsymbol{H} - \boldsymbol{H}_{hp}^{[M]}\right\|_{\boldsymbol{H}(\mathrm{curl})}$ with *hp*-refinement.

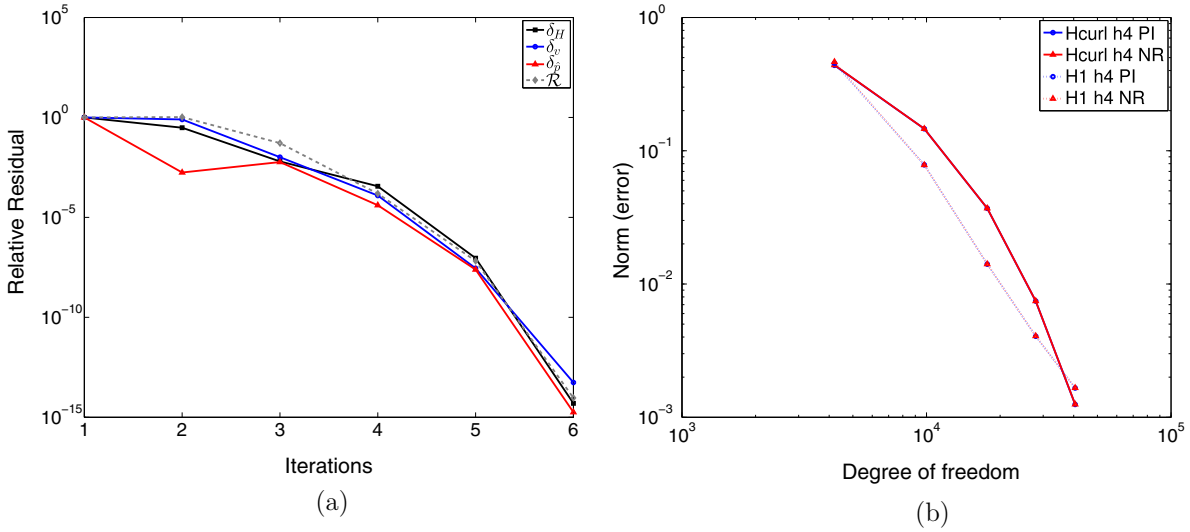

Fig. 6. Two-dimensional rectangular domain with Hartmann flow with $Ha = 10$, showing: (a) the typical quadratic convergence for updates $\boldsymbol{\delta}_v, \delta_{\hat{p}}$ and δ_H and the relative residual $\mathcal{R}$ for the Newton–Raphson implementation for uniform $p = 7$ elements and (b) the convergence of $\left\|\boldsymbol{v} - \boldsymbol{v}_{hp}^{[M]}\right\|_{H^1}$ and $\left\|\boldsymbol{H} - \boldsymbol{H}_{hp}^{[M]}\right\|_{\boldsymbol{H}(\mathrm{curl})}$ for Newton–Raphson and $\left\|\boldsymbol{\delta}_v - \boldsymbol{\delta}_{v,hp}^{[0]}\right\|_{H^1}$ and $\left\|\boldsymbol{\delta}_H - \boldsymbol{\delta}_{H,hp}^{[0]}\right\|_{\boldsymbol{H}(\mathrm{curl})}$ for one-step Picard.

Table 1

Two-dimensional rectangular domain with Hartmann flow showing: the convergence with $Ha = 10$ for $h = 0.25$. $\left(\text{Here } E(\boldsymbol{v})_{H^1} = \left\|\boldsymbol{v} - \boldsymbol{v}_{hp}^{[M]}\right\|_{H^1}, E(\boldsymbol{v})_{L_2} = \left\|\boldsymbol{v} - \boldsymbol{v}_{hp}^{[M]}\right\|_{L_2}, E(\hat{p})_{L_2} = \left\|\hat{p} - \hat{p}_{hp}^{[M]}\right\|_{L_2}, E(\boldsymbol{H})_{\boldsymbol{H}(\mathrm{curl})} = \left\|\boldsymbol{H} - \boldsymbol{H}_{hp}^{[M]}\right\|_{\boldsymbol{H}(\mathrm{curl})}\right)$.

p	Dofs in $\boldsymbol{H}_{hp}/r_{hp}/\boldsymbol{v}_{hp}/\hat{p}_{hp}$	$E(\boldsymbol{v})_{H^1}$	$E(\boldsymbol{v})_{L_2}$	$E(\hat{p})_{L_2}$	$E(\boldsymbol{H})_{\boldsymbol{H}(\mathrm{curl})}$
3	2880/1681/3454/1200	7.64E−02	2.45E−02	1.22E−03	4.34E−03
4	5440/3041/6206/2400	1.46E−02	2.09E−03	2.17E−04	1.11E−03
5	8800/4801/9758/4000	2.43E−03	2.13E−04	3.34E−05	2.25E−04
6	12,960/6961/14,110/6000	3.46E−04	2.45E−05	4.82E−06	3.77E−05
7	17,920/9521/19,262/8400	4.42E−05	2.65E−06	7.98E−07	5.39E−06

Table 2

As Table 1 but for $h = 0.125$.

p	Dofs in $\boldsymbol{H}_{hp}/r_{hp}/\boldsymbol{v}_{hp}/\hat{p}_{hp}$	$E(\boldsymbol{v})_{H^1}$	$E(\boldsymbol{v})_{L_2}$	$E(\hat{p})_{L_2}$	$E(\boldsymbol{H})_{\boldsymbol{H}(\mathrm{curl})}$
3	12,900/7645/15,478/5256	1.12E−02	1.92E−03	1.43E−04	1.26E−03
4	24,208/13,697/27,646/10,512	1.03E−03	6.18E−05	1.38E−05	1.58E−04
5	39,020/21,501/43,318/17,520	8.43E−05	3.54E−06	1.31E−06	1.55E−05
6	57,336/31,057/62,494/26,280	6.46E−06	2.21E−07	1.57E−07	1.28E−06
7	79,156/42,365/85,174/36,792	5.51E−07	1.51E−08	2.15E−08	9.21E−08

5.1.3. Fully coupled non-linear square domain smooth problem

A fully coupled non-linear MHD problem with a known smooth analytical solution can be found in several references such as [18,9]. We use the former for benchmarking our fully coupled Newton–Raphson implementation summarised in Algorithm 1. The geometry consists of a square domain $\Omega = (-1, 1)^2$, and we construct the problem by setting the parameters as $[[\mu_r]] = [[\mathbb{I}]], c[[\tilde{\sigma}]]^{-1} = 10^4$ and $\rho = \hat{\mu} = 1$. The source terms $\tilde{\boldsymbol{f}}, \boldsymbol{g}$ are chosen so that the analytical solution is

$$\boldsymbol{v} = \begin{pmatrix} y^2 \\ x^2 \end{pmatrix}, \quad \hat{p} = x, \qquad \boldsymbol{H} = \begin{pmatrix} 1 - y^2 \\ 1 - x^2 \end{pmatrix}, \quad r = (1 - x^2)(1 - y^2). \tag{27}$$

in Ω and the Dirichlet boundary conditions $\boldsymbol{v}_{hp}^{[0]} = \boldsymbol{v}$ on $\partial\Omega_D^F = \partial\Omega$ and $\boldsymbol{n} \times \boldsymbol{H}_{hp}^{[0]} = \boldsymbol{n} \times \boldsymbol{H}$ on $\partial\Omega_D^M = \partial\Omega$ are applied. From (27), we can deduce that, of the different fields, r is of the highest polynomial degree being bi-quadratic and, for triangular elements, this means that $p = 4$ H^1 conforming elements are required to fully capture this field. Although $\boldsymbol{H}$ and $\boldsymbol{v}$ are quadratic functions, which can be captured with $p = 2$ H^1 conforming and $p = 2$ $\boldsymbol{H}(\mathrm{curl})$ conforming elements, respectively, we expect that, due to the coupled nature of the problem, these fields will not be fully resolved until the degree is $p = 4$ (using our earlier naming convention).

For the fully coupled smooth problem, we consider performing hp-refinement with elements of uniform size $h = 0.6, 0.3, 0.15, 0.075$, the finest mesh having 2048 unstructured triangular elements. Uniform p-refinement is applied with polynomial degrees $p = 2, 3, 4, 5$, where the last p increment represents an intentional overkill to test the implementation.

In Fig. 5(a) we show the computed quadratic convergence for updates $\boldsymbol{\delta}_{v,hp}^{[m]}, \boldsymbol{\delta}_{H,hp}^{[m]}$ and $\delta_{\hat{p},hp}^{[m]}$ and the relative residual $\mathcal{R} = \|\mathcal{R}_v^{[m]}, \mathcal{R}_{\hat{p}}^{[m]}, \mathcal{R}_H^{[m]}, \mathcal{R}_r^{[m]}\| / \|\mathcal{R}_v^{[0]}, \mathcal{R}_{\hat{p}}^{[0]}, \mathcal{R}_H^{[0]}, \mathcal{R}_r^{[0]}\|$ for $p = 5$ elements,

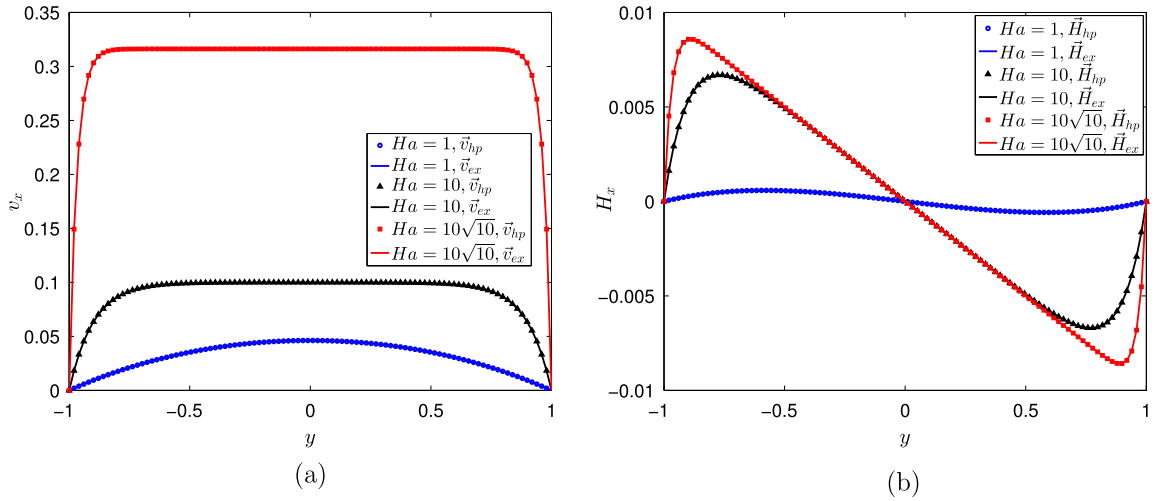

Fig. 7. Two-dimensional rectangular domain with Hartmann flow showing: Centreline profiles for (a) v_x and (b) H_x for $Ha = 1, 10, 10\sqrt{10}$ on an unstructured mesh of 400 triangular elements and uniform polynomial degree $p = 7$.

which implies the correct implementation of the Newton–Raphson method. Then, in Fig. 5(b) we show the convergence of *hp*-refinement for $\|\boldsymbol{v} - \boldsymbol{v}_{hp}^{[m]}\|_{H^1}, \|\hat{p} - \hat{p}_{hp}^{[m]}\|_{L_2}$ and $\|\boldsymbol{H} - \boldsymbol{H}_{hp}^{[m]}\|_{\boldsymbol{H}(\mathrm{curl})}$ with $m = M$, such that $\mathcal{R} \leqslant 10^{-10}$, which indicate a downward sloping curve confirming the expected exponential convergence of *p*-refinement for each of the meshes considered. Note that, unless otherwise stated, this Newton–Raphson convergence criteria will be used in the following. As the analytical solution for r is bi-quadratic, the *p*-refinement should converge to machine precision with $p = 4$ for this problem, which is exactly exhibited in the figure.

5.1.4. The two-dimensional Hartmann flow problem

The description of the $d = 2$ Hartmann flow problem can be found in [18,9] and this allows us to further benchmark our full Newton–Raphson scheme as the resulting solution satisfies both the linearised and the non-linear MHD equations. For this problem, the domain is set to be $\Omega = (0, L) \times (-1, 1)$ with $L \gg 1$, for which we choose $L = 10$. The analytical solution corresponds to an unidirectional flow under constant pressure gradient $-G$ in the x-direction with $\tilde{\boldsymbol{f}} = \boldsymbol{g} = \boldsymbol{0}$. In order to apply our scheme to the reference non-dimensional Hartmann flow problem, we set the parameters as $[[\mu_r]] = [[\mathbb{I}]], \nu = \hat{\mu}/\rho = 0.1, [[\tilde{\sigma}]] = \tilde{\sigma}[[\mathbb{I}]], \tilde{\sigma}^{-1}c/\rho = 0.1$, $Ha = 10, G = 0.5, \rho = 1, p_0 = 10$. The analytical solution to this problem then corresponds to

$$\boldsymbol{v} = \begin{pmatrix} \frac{G}{\mu\nu Ha \tanh(Ha)} \left(1 - \frac{\cosh(yHa)}{\cosh(Ha)}\right) \\ 0 \end{pmatrix}, \tag{28}$$

$$\boldsymbol{H} = \begin{pmatrix} \frac{G}{\rho} \left(\frac{\sinh(yHa)}{\sinh(Ha)} - y\right) \\ 1 \end{pmatrix}, \tag{29}$$

$$\hat{p} = -Gx - \frac{G^2}{2\rho} \left(\frac{\sinh(yHa)}{\sinh(Ha)} - y\right)^2 + p_0, \tag{30}$$

$$r = 0. \tag{31}$$

in Ω. We set $\partial\Omega_D^F$ to be the boundaries corresponding to $(0, y), y \in (0, 1)$ and $(x, \pm 1), x \in (0, L)$ and here we prescribe $\boldsymbol{v}_{hp}^{[0]} = \boldsymbol{v}$ and we set $\partial\Omega_D^M = \partial\Omega$ and $\boldsymbol{n} \times \boldsymbol{H}_{hp}^{[0]} = \boldsymbol{n} \times \boldsymbol{H}$, while on $\partial\Omega_N^F = \partial\Omega \setminus \partial\Omega_D^F$, we prescribe $\boldsymbol{t}_{hp} = \boldsymbol{t} = [[\sigma_{EM}]]\boldsymbol{n}$ (free velocity boundary), based on the above analytical solution.

As the analytical solution is smooth for this low Hartmann number, a single mesh consisting of 400 triangular elements is

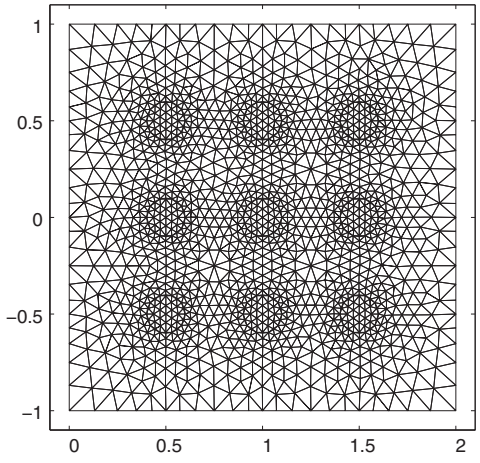

Fig. 8. Two-dimensional multiphase duct flow problem showing: geometry and mesh with 2910 unstructured triangular elements for duct flow problem.

Table 3
Two-dimensional multiphase duct flow problem showing: parameters for inside and outside MHD fluids.

Parameters	Inner fluid	Outer fluid
ρ (kg m^{-3})	2700	1000
$\hat{\mu}$ (N s m^{-2})	0.3	0.1
$c\tilde{\sigma}^{-1}$ (A V kg^{-1} s^2)	$10\mu_0$	$0.1\mu_0$
μ_r	1.002	0.99
$\mu_r^{(1)}$	0.01	0.01
$\mu_r^{(2)}$	0.01	0.01

employed. On this mesh we consider both the linearised one step Picard [23] and the fully coupled non-linear Newton–Raphson schemes. For the one-step Picard scheme we solve the linearised problem, as described in [23], and for the Newton–Raphson scheme we apply Algorithm 1. In both cases, we apply uniform *p*-refinement with polynomial degrees $p = 3, 4, 5, 6, 7$ and show, in Fig. 6(a), the typical quadratic convergence of the relative residual $\mathcal{R} = \|\mathcal{R}_v^{[m]}, \mathcal{R}_{\hat{p}}^{[m]}, \mathcal{R}_H^{[m]}, \mathcal{R}_r^{[m]}\| / \|\mathcal{R}_v^{[0]}, \mathcal{R}_{\hat{p}}^{[0]}, \mathcal{R}_H^{[0]}, \mathcal{R}_r^{[0]}\|$ for the Newton–Raphson iterations when uniform $p = 7$ elements are used. In Fig. 6(b), we show the convergence of $\|\boldsymbol{v} - \boldsymbol{v}_{hp}^{[M]}\|_{H^1}$

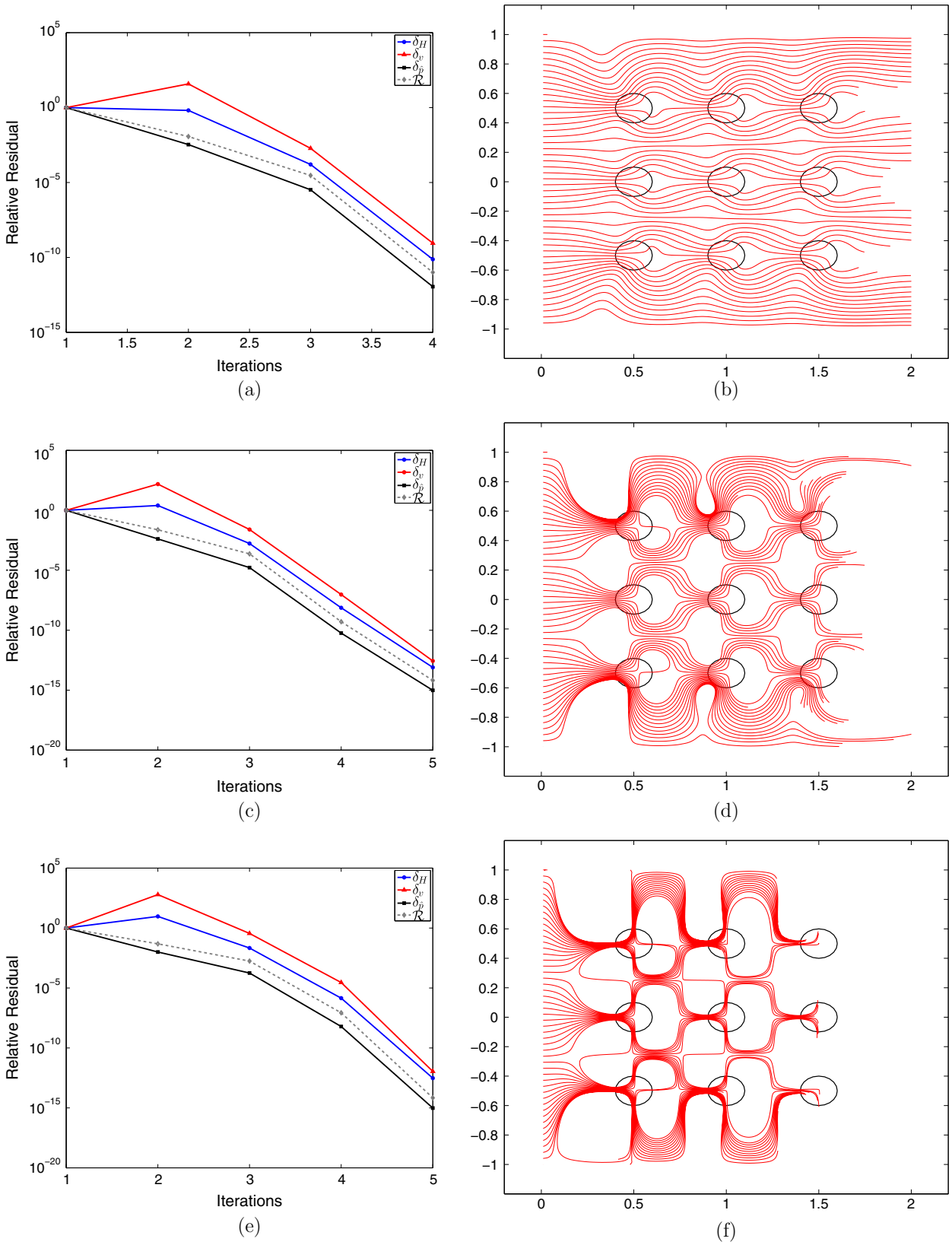

Fig. 9. Two-dimensional multiphase duct flow problem showing: (a), (c), (e) the quadratic convergence for updates $\boldsymbol{\delta}_v, \delta_{\tilde{p}}$ and δ_H and the relative residual $\mathcal{R}$ of the Newton–Raphson implementation for uniform $p = 5$ elements with $H = 0.1, 0.2, 0.4$, respectively, and (b), (d), (f) the corresponding streamlines.

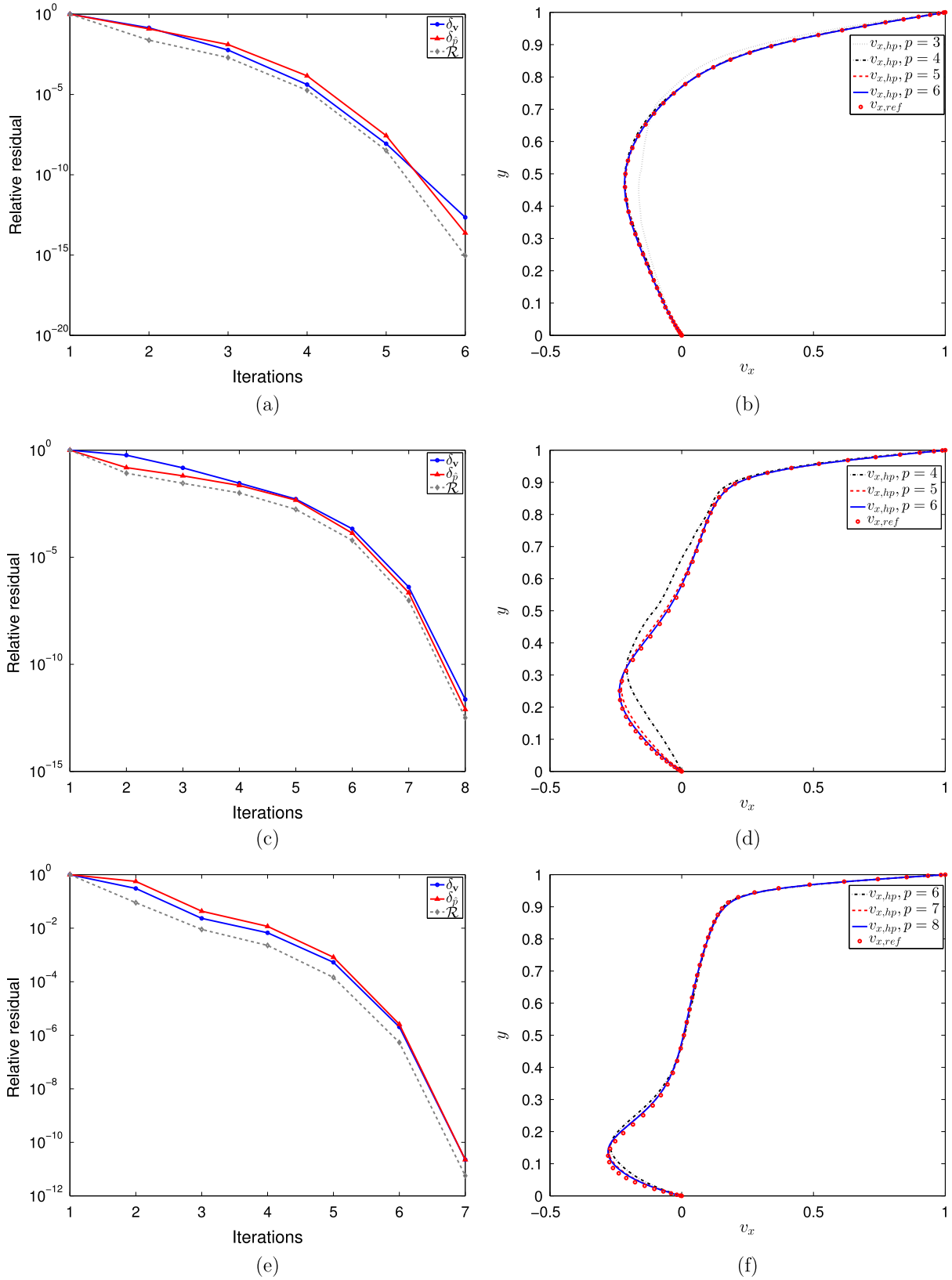

Fig. 10. Three-dimensional lid-driven cavity problem showing: (a), (c), (e) the typical quadratic convergence for $\boldsymbol{\delta}_v, \delta_{\tilde{p}}$ and $\mathcal{R}$ for Newton–Raphson implementation for $Re = 100, 400, 1000$ with $p = 6, 6, 8$, respectively, and (b), (d), (f) the centreline profiles of $v_x(0.5, y, 0.5)$ for $0 \leqslant y \leqslant 1$ for $Re = 100, 400, 1000$ with p-refinement, respectively, and comparisons with the reference solutions [39].

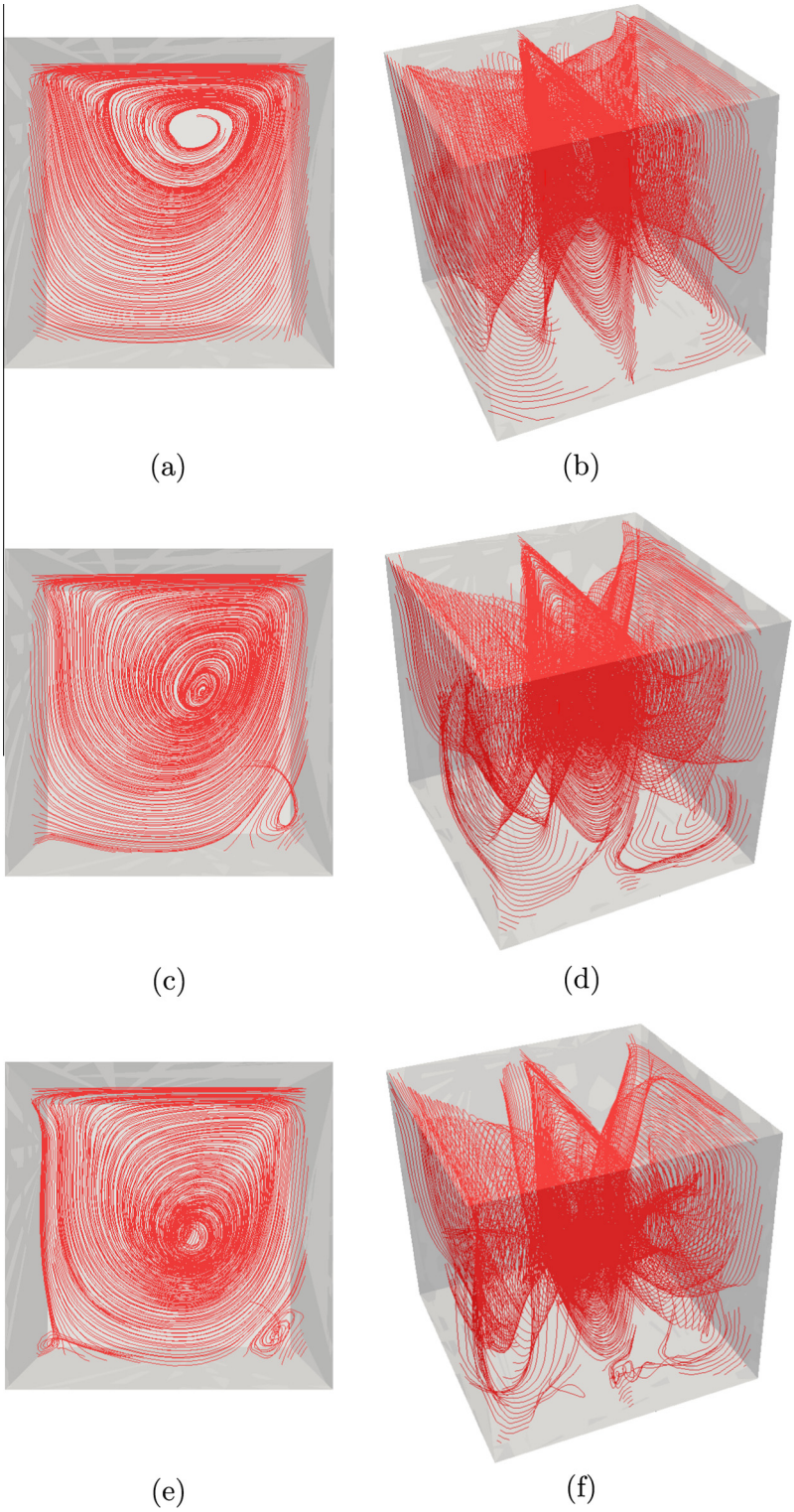

Fig. 11. Three-dimensional lid-driven cavity problem showing: (a), (b) the streamlines for $Re = 100$ with $p = 6$, (c), (d) the streamlines for $Re = 400$ with $p = 6$, (e), (f) the streamlines for $Re = 1000$ with $p = 8$.

and $\|\boldsymbol{H} - \boldsymbol{H}_{hp}^{[M]}\|_{\boldsymbol{H}(\mathrm{curl})}$ where M denotes the iteration of the converged solution for Newton–Raphson scheme and $\|\boldsymbol{\delta}_{\nu} - \boldsymbol{\delta}_{\nu,hp}^{[0]}\|_{H^1}$ and $\|\boldsymbol{\delta}_{H} - \boldsymbol{\delta}_{H,hp}^{[0]}\|_{\boldsymbol{H}(\mathrm{curl})}$ for the one-step Picard. Fig. 6(b), indicates that both schemes converge exponentially fast with p-refinement to the analytical solution.

Subsequently, we have considered the convergence of updates $\|\boldsymbol{v} - \boldsymbol{v}_{hp}^{[M]}\|_{L_2}, \|\boldsymbol{v} - \boldsymbol{v}_{hp}^{[M]}\|_{H^1}, \|\hat{p} - \hat{p}_{hp}^{[M]}\|_{L_2}$ and $\|\boldsymbol{H} - \boldsymbol{H}_{hp}^{[M]}\|_{\boldsymbol{H}(\mathrm{curl})}$ for Hartmann numbers $Ha = 0.01, 1, 10, 10\sqrt{10}$ under hp-refinements. These tabulated results are presented in full in [24], here we show only the case for $Ha = 10$ for $h = 0.25$ and $h = 0.125$ in Tables 1

Table 4
Three-dimensional lid-driven cavity problem with a magnetic field applied showing: the parameters for the problem with Hartmann number $Ha = 10$.

Ha	ν	ν_m	κ	μ_r
10	0.0025	0.025	0.00625	1

and 2, respectively, which we compare with the convergence of the error stated in references [18,9].

Although the results shown in [18,9] are obtained with a different method and are presented for *h*-refinement only, we can compare the accuracy of the solutions with respect to the number of degrees of freedom (DOFs). Our *hp*-finite element scheme shows a significant improvement in terms of accuracy when compared to the reference solution. In particular, we can use much fewer DOFs yet still achieve the same level of accuracy, which indicates the high efficiency and high accuracy of the current approach. However, we also acknowledge that, ideally, if the data is available, the computational cost should not only be measured in terms of degrees of freedom as a *hp*-approach does result in matrices that are not as sparse as in pure *h*-refinement and there are additional computation costs associated with the generation of the basis functions and the evaluation of the elemental contributions. Nonetheless, these can be minimised by a careful implementation, see e.g. [24]. From the tables of convergence behaviour in [24], we also can conclude that, for higher Hartmann number, more DOFs are needed. This indicates that a high Hartmann number introduces strong coupling, steeper gradients as well as non-linearity into the system, which makes the flow behaviour much more challenging to capture.

The numerical solutions for the centreline profiles for *x*-component of the velocity and *x*-component of the magnetic field are illustrated in Fig. 7 with different Hartmann numbers. It transpires that, on the chosen mesh, the degree of the elements needs to be chosen as $p = 7$ to fully capture the behaviour of the strong coupling and the non-linearity of the MHD problem. The comparison between numerical and analytical solutions, which shows a good agreement, indicates the accuracy of the implementation. From the results, we can also see that, a high Hartmann number results in steeper gradients near the boundary, which are well captured by our *hp*-refinements.

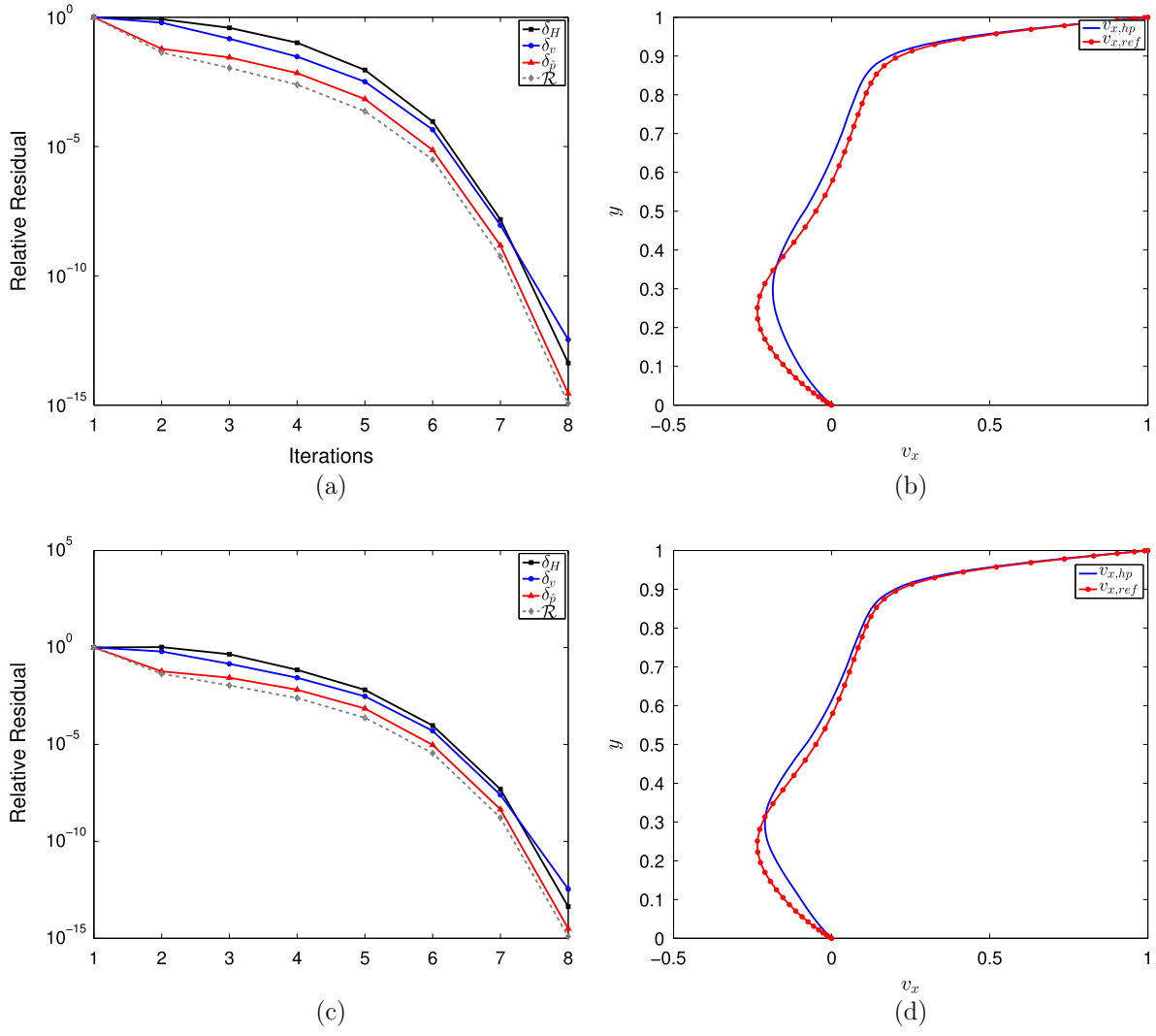

Fig. 12. Three-dimensional lid-driven cavity flow problem with a magnetic field showing: (a), (c) the typical quadratic convergence of updates $\boldsymbol{\delta}_v, \delta_{\tilde{p}}$ and δ_H and relative residual $\mathcal{R}$ for $Ha = 10$ with $\boldsymbol{H}_D = (1, 0, 0)$ and $\boldsymbol{H}_D = (0, 1, 0)$, respectively, for uniform $p = 4$ elements and (b), (d) the centreline profiles of $v_x(0.5, y, 0.5)$ for $0 \leqslant y \leqslant 1$ compared with a reference solution in absence of the magnetic field [39].

5.1.5. Two-dimensional duct flow with cylinder shaped different media inside

After verifying our implementation, and in order to show the applicability of our approach to capture complex flow patterns, we now consider applying Algorithm 2 to solve a multiphase MHD flow, which consists of two different fluids. The geometry and mesh are shown in Fig. 8. The mesh is refined near the inner droplet as we are interested in the behaviour between two different fluids.

The domain consists of $\Omega = (0,2)\times(-1,1)$ with 9 droplets, each being a circle with radius $r_{in} = 0.1$ and equally separated inside the squared domain at positions $(0.5,-0.5),(0.5,0),(0.5,0.5),(1,-0.5),(1,0),(1,0.5),(1.5,-0.5),(1.5,0)$ and $(1.5,0.5)$. The Neumann boundary for the fluid part is $\partial\Omega_N^F = (2,y), y\in(-1,1)$ with condition $\boldsymbol{t}_{hp} = \boldsymbol{t} = [[\sigma_{EM}]]\boldsymbol{n}$ and the Dirichlet boundary for the fluid part $\partial\Omega_D^F = \partial\Omega\setminus\partial\Omega_N^F$ with condition $\boldsymbol{v}_{hp}^{[0]} = (v(1-y^2),0)$. For the magnetic field, the Dirichlet boundary conditions $\boldsymbol{n}\times\boldsymbol{H}_{hp}^{[0]} = \boldsymbol{n}\times\boldsymbol{H}_D$ are applied on $\partial\Omega_D^M = \partial\Omega$ where $\boldsymbol{H}_D = (0,H)$. Note that v is the amplitude of input velocity and H is the amplitude of the magnetic field. In order to investigate the influence of the magnetic field on the multiphase problem, the amplitude H of the magnetic field is increased. The parameters for the inner and outer fluids are taken from [13,15] and shown in Table 3. Here v can be obtained by the relation $v = Re\times\hat{\mu}/(2r_{in})$, where $Re = 0.01$ is the Reynolds number without the magnetic field and in absence of the droplets.

With a mesh of 2910 unstructured triangular elements, we found, by uniformly incrementing the polynomial degree, that $p = 5$ is required in order to fully capture the complex fluid pattern. Several different magnetic amplitudes are applied, namely $H = 0.1, 0.2, 0.4$, and the results of the streamlines for the multiphase problem and the quadratic convergence curve for the different magnetic fields are shown in Fig. 9. The results shown in Fig. 9 (a), (c), and (d) indicate the correct implementation of the Newton–Raphson scheme and in Fig. 9(b), (d), and (e) the influence of the magnetic field over the fluid flow pattern is illustrated. In particular, we see that as the magnitude of the magnetic field is increased, the flow pattern is substantially effected creating regions of low and high velocities in the vicinity of the conducting cylinders. This complex flow pattern would be impossible to be captured without the use of a higher order discretisation. Fig. 9 also indicates that the contrast of the magnetic permeability for the two different fluids could result in a complex flow pattern under a large magnetic field.

Table 5
Three-dimensional rectangular domain with Hartmann flow showing: the parameters for Hartmann flow problem with various Hartmann numbers $Ha = 0.01, 1, 10, 10\sqrt{10}$.

Ha	ν	ν_m	κ	G
0.01	1	1e4	1	0.5
1	1	10	10	0.1
10	0.1	1	10	0.1
$10\sqrt{10}$	0.01	1	10	0.1

5.2. Three-dimensional problems

Next, we verify the $d = 3$ implementation by applying the scheme to several well-known benchmarking problems. As we have already established the benefits of the Newton Raphson over the Picard iteration we consider only the former and use it to benchmark a lid-driven cavity with and without a magnetic field, a three dimensional extension of the Hartmann flow problem and, to finish, we show the predicative capability of the scheme by applying it to a multiphase MHD flow problem.

5.2.1. The three-dimensional lid-driven cavity problem

We first consider the standard lid-driven cavity problem for pure Navier–Stokes flow in the absence of a magnetic field on the cubic domain $\Omega = (0,1)^3$. We define the surface $(x,y,1), x,y\in(0,1)$ as $\partial\Omega_D^{F(1)}$ and the other boundary faces as $\partial\Omega_D^{F(2)} = \partial\Omega\setminus\partial\Omega_D^{F(1)}$. We impose the boundary conditions

$$\boldsymbol{v} = (v,0) \quad \text{on } \partial\Omega_D^{F(1)},$$
$$\boldsymbol{v} = \boldsymbol{0} \quad \text{on } \partial\Omega_D^{F(2)}.$$

where v is the constant amplitude of the applied of the driving velocity. For this problem an unstructured mesh of 756 tetrahedral elements is generated on which uniform order $p = 3,4,5,6$ elements are applied for $Re = 100$, $p = 4,5,6$ are applied for $Re = 400$ and $p = 6,7,8$ are applied for $Re = 1000$.

Initially, we consider the flow pattern in the absence of a magnetic field. Fig. 10(a), (c), and (e) shows the quadratic convergence of a suitably simplified version of the Newton–Raphson procedure given in Algorithm 1 to the previously stated criteria where $\mathcal{R} = \|\mathcal{R}_v^{[m]}, \mathcal{R}_p^{[m]}\|/\|\mathcal{R}_v^{[0]}, \mathcal{R}_p^{[0]}\|$ and the convergence of the updates variables $\boldsymbol{\delta}_v$ and $\boldsymbol{\delta}_p$ are also presented for completeness. We can observe that, with an increasing Reynolds number, we need more iterations to converge. For $Re = 1000$, an incremental approach

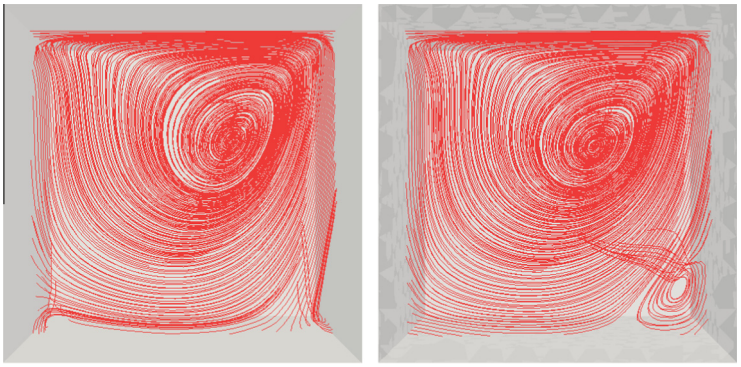

(a) (b)

Fig. 13. Three-dimensional lid-driven cavity flow problem with a magnetic field showing: (a) and (b) the streamlines for $Ha = 10$ with $\boldsymbol{H}_D = (1,0,0)$ and $\boldsymbol{H}_D = (0,1,0)$, respectively, for uniform $p = 4$ elements.

using 2 increments has also been applied (see [24] for details). Note that the convergence shown in Fig. 10(e) is for the final increment for $Re = 1000$ with $p = 8$. In Fig. 10(b), (d), and (f), the centreline profiles for $v_x(0.5, y, 0.5)$ for $0 \leqslant y \leq 1$ for $Re = 100, 400, 1000$ with p-refinement are presented and in Fig. 11 the corresponding streamlines are shown. The results show that as the degree of the polynomial order is increased, the solution converges to the reference solution. For the lower Reynolds number $Re = 100$ we can see that, with $p = 4$, we can already accurately capture the fluid behaviour. For $Re = 400, p = 6$ is needed to fully solve the problem. For $Re = 1000$, even with $p = 8$, our computed solution is still slightly away from the reference solution. In this case local mesh refinement, combined with p-refinement could be applied, if desired, to improve the accuracy.

Secondly, we consider the case of the coupled MHD problem where, in addition to the fluid boundary conditions, we apply $\boldsymbol{n} \times \boldsymbol{H}_{hp}^{[0]} = \boldsymbol{n} \times \boldsymbol{H}_D$ on $\partial\Omega_D^M = \partial\Omega$ where we choose $\boldsymbol{H}_D = (1, 0, 0)$ and $\boldsymbol{H}_D = (0, 1, 0)$, in turn, as uniform magnetic fields. Here, in order to adapt our framework to the dimensionless schemes, we set the parameters as $[[\mu_r]] = [[\mathbb{I}]], \kappa = \rho, \nu = \hat{\mu}/\rho = 0.1, [[\tilde{\sigma}]] = \tilde{\sigma}[[\mathbb{I}]], \nu_m = \tilde{\sigma}^{-1}c/\rho, Ha = \sqrt{\kappa/\nu\nu_m}$. The fluid parameters are summarised in Table 4 for the Hartmann number $Ha = 10$ with $Re = 1/\nu = 400$ and $Rem = 1/\nu_m = 40$ as [2]. The mesh of 6048 unstructured tetrahedra is employed and uniform $p = 4$ elements are used throughout. In Fig. 12(a) and (c) we show the quadratic convergence of the Newton–Raphson procedure given in Algorithm 1 to the previously stated criteria and in Fig. 12(b) and (d), the centreline profiles of $v_x(0.5, y, 0.5)$ for $0 \leqslant y \leqslant 1$ for $Ha = 10$ when $\boldsymbol{H}_D = (1, 0, 0)$ and $\boldsymbol{H}_D = (0, 1, 0)$ are shown. In the latter cases, we also include the corresponding reference solution for the Navier–Stokes lid driven cavity problem with $Re = 400$ as a comparison. Illustrations of the computed streamlines for this problem are presented in Fig. 13. Note that, for further increases in Hartmann number, we see an even greater departure of the flow field for the MHD problem from the flow field of the standard lid driven cavity problem [24].

5.2.2. The three-dimensional Hartmann flow problem

The description of this problem can be found in [18,9] and consists of a rectangular duct given by $\Omega = (0, L) \times (-y_0, y_0) \times (-z_0, z_0)$ with $y_0, z_0 \ll L$. The source terms are $\tilde{\boldsymbol{f}} = \boldsymbol{g} = \boldsymbol{0}$ and the analytical solutions is in the form of

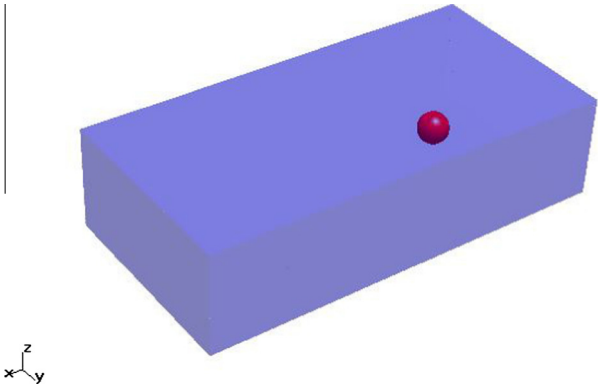

Fig. 15. Three-dimensional multiphase duct flow problem showing: the geometry.

$$\boldsymbol{v} = \begin{pmatrix} v(y,z) \\ 0 \\ 0 \end{pmatrix}, \quad \boldsymbol{H} = \begin{pmatrix} b(y,z) \\ 1 \\ 0 \end{pmatrix},$$

$$\hat{p} = -Gx + \hat{p}_0(y,z), \quad r = 0.$$

in Ω where

$$v(y,z) = -\frac{1}{2}G\nu^{-1}(z^2 - z_0^2) + \sum_{n=0}^{+\infty} v_n(y)\cos(\lambda_n z),$$

$$b(y,z) = \sum_{n=0}^{+\infty} b_n(y)\cos(\lambda_n z),$$

$$\hat{p}_0(y,z) = -\frac{\kappa b(y,z)^2}{2} + 10,$$

and

$$\lambda_n = \frac{(2n+1)\pi}{2z_0},$$

$$b_n(y) = \frac{\nu}{\kappa}\left(A_n \frac{\lambda_n^2 - p_1^2}{p_1}\sinh(p_1 y) + B_n \frac{\lambda_n^2 - p_2^2}{p_2}\sinh(p_2 y)\right),$$

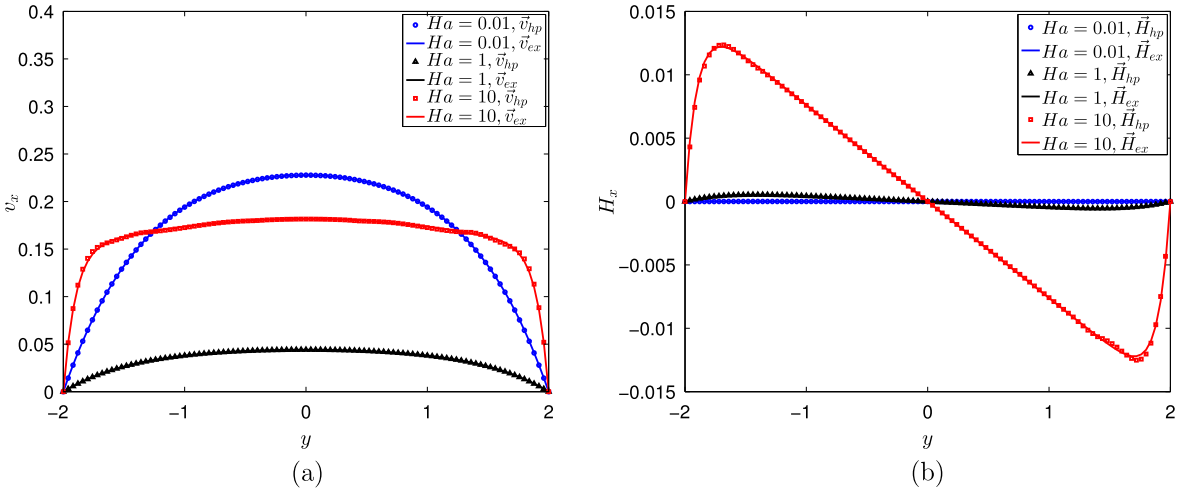

Fig. 14. Three-dimensional rectangular domain with Hartmann flow showing: (a) the centreline profiles of $v_x(5, y, 0)$ and (b) $H_x(5, y, 0)$ for $-2 \leqslant y \leqslant 2$ for Hartmann numbers $Ha = 0.01, 1$ and 10 with uniform $p = 6$ elements.

$$p_{1,2}^2 = \lambda_n^2 + \frac{Ha^2}{2} \pm Ha\sqrt{\lambda_n^2 + \frac{Ha^2}{4}},$$

$$A_n = \frac{-p_1(\lambda_n^2 - p_2^2)}{\Delta_n} u_n(y_0)\sinh(p_2 y_0),$$

$$B_n = \frac{-p_2(\lambda_n^2 - p_1^2)}{\Delta_n} u_n(y_0)\sinh(p_1 y_0),$$

$$\Delta_n = p_2(\lambda_n^2 - p_1^2)\sinh(p_1 y_0)\cosh(p_2 y_0) - p_1(\lambda_n^2 - p_2^2)\sinh(p_2 y_0) \times \cosh(p_1 y_0),$$

$$v_n(y_0) = \frac{-2G}{v\lambda_n^3 z_0}\sin(\lambda_n z_0),$$

In order to again adapt our framework to the dimensionless Hartmann flow problem, we set the parameters as $[[\mu_r]] = [[\mathbb{I}]]$, $\kappa = \rho, \nu = \hat{\mu}/\rho = 0.1, [[\tilde{\sigma}]] = \tilde{\sigma}[[\mathbb{I}]], v_m = \tilde{\sigma}^{-1}c/\rho, Ha = \sqrt{\kappa/\nu v_m}$. The fluid parameters for the three-dimensional Hartmann flow problem for different Hartmann numbers of $Ha = 0.01, 1, 10, 10\sqrt{10}$ are shown in Table 5. Then, following the literature [18,9,13], we consider the solution of this problems for the dimensionless quantities $L = 10, y_0 = 2$ and $z_0 = 1$. The fluid Neumann boundary $\partial\Omega_N^F$ is set as the face $(10, y, z), (y, z) \in (-y_0, y_0) \times (-z_0, z_0)$ and the fluid Dirichlet boundary $\partial\Omega_D^F$ as $\partial\Omega_D^F = \partial\Omega \setminus \partial\Omega_N^F$ and, for the magnetic field, we set $\partial\Omega_D^M = \partial\Omega$. Introducing $\boldsymbol{H}_D = (0, 1, 0)$ the boundary conditions can be summarised as

$$\boldsymbol{v}_{hp}^{[0]} = 0 \qquad \text{on } \partial\Omega_D^F,$$

$$\boldsymbol{t}_{hp} = ([[\sigma_F]] + [[\sigma_{EM}]])\boldsymbol{n} = \hat{p}_0\boldsymbol{n} + [[\sigma_{EM}]]\boldsymbol{n} \qquad \text{on } \partial\Omega_N^F,$$

$$\boldsymbol{n} \times \boldsymbol{H}_{hp}^{[0]} = \boldsymbol{n} \times \boldsymbol{H}_D \qquad \text{on } \partial\Omega_D^M.$$

The benchmarking is performed on an unstructured grid of 125 elements by performing uniform p-refinement. By uniformly increasing p until convergence was reached, it was deduced that using $p = 6$ on a mesh of 125 elements can capture the Hartmann flow pattern accurately for the Hartmann number up to $Ha = 10$. By applying Algorithm 1 the Newton–Raphson procedure exhibits quadratic convergence similar to that shown in the previous cases, although, for higher Hartmann numbers, the number of iterations required to reach the aforementioned convergence criteria increases.

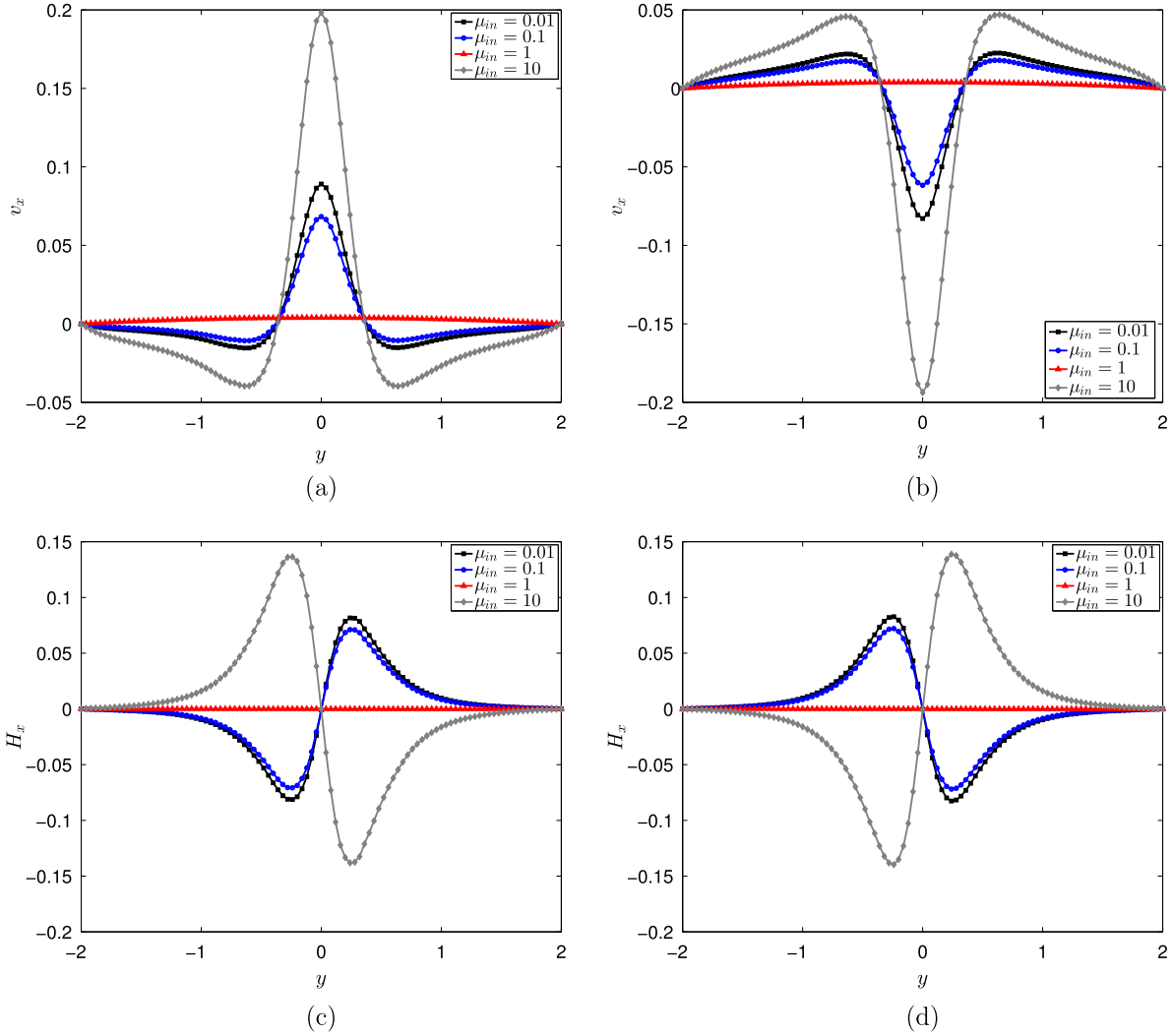

Fig. 16. Three-dimensional multiphase duct flow problem showing: (a) and (b) centreline profiles for $v_x(-1.5, y, 0), v_x(2.5, y, 0)$, respectively, for $-2 \leqslant y \leqslant 2$ when $\mu_{rin} = 0.01, 0.1, 1, 10$ and (c), (d) centreline profiles for $H_x(-1.5, y, 0)$ and $H_x(2.5, y, 0)$, respectively, for the same problem.

The centreline profiles of $v_x(5,y,0)$ and $H_x(5,y,0)$ for $-2 \leqslant y \leqslant 2$ are illustrated in Fig. 14 for the Hartmann numbers $Ha = 0.01, 1$ and 10. The comparison between the numerical solutions and the analytical solutions show a good agreement for the presented cases. For higher Hartmann numbers the flow patterns exhibit increasingly sharp gradients in the flow field close to the boundaries and, as discussed in [24] performing p-refinement alone on a coarse mesh of 125 tetrahedra is not sufficient to capture the flow pattern. In this case, h- and p-refinements must be combined.

5.2.3. The three dimensional multi-phase MHD flow problem

The geometry of the multiphase MHD flow is shown in Fig. 15, which is a rectangular duct given by $\Omega = (0,L) \times (-y_0,y_0) \times (-z_0,z_0)$ with dimensionless coordinates $y_0 = 2, z_0 = 1, L = 8$ containing a sphere with radius 0.3 at the point of $(2,0,0)$. The source terms are such that $\tilde{\boldsymbol{f}} = \boldsymbol{g} = \boldsymbol{0}$ and the fluid Neumann boundary condition $\boldsymbol{t}_{hp} = \boldsymbol{t} = [[\sigma_{EM}]]\boldsymbol{n}$ (free stream velocity) is applied at the face $(8,y,z)$ with $(y,z) \in (-y_0,y_0) \times (-z_0,z_0)$ and the fluid Dirichlet boundary conditions $\boldsymbol{v}_{hp}^{[0]} = \boldsymbol{v}_D$ where $\boldsymbol{v}_D = (0.001(2+y)(2-y),0,0)$ is a Poiseuille flow distribution in the x-direction. For the magnetic field, the boundary condition $\boldsymbol{n} \times \boldsymbol{H}_{hp}^{[0]} = \boldsymbol{n} \times \boldsymbol{H}_D$ is imposed on $\partial\Omega_D^M = \partial\Omega$ where $\boldsymbol{H}_D = (0,H,0)$. The parameters are taken to be same as those previously provided in Table 5, except that we assign the background fluid such that, in absence of the inclusion, the Hartmann number would be $Ha = 1$ and in absence of the background the Hartmann number would be $Ha = 10\sqrt{10}$. We fix the relative permeability of the background fluid to be $\mu_{rout} = 1$ whilst varying the relative permeability of the inner fluid droplet according to $\mu_{rin} = 0.01, 0.1, 1, 10$, in turn. For both fluids we set $\mu_r^{(1)} = \mu_r^{(2)} = 0$.

By uniformly incrementing p on an unstructured grid of 1765 tetrahedral elements it was found that convergence is reached with $p = 4$ elements. As in previous cases, the application of Algorithm 2 results in a Newton–Raphson scheme that converges quadratically exhibiting a behaviour similar to that shown in earlier plots. In Fig. 16 we also present the centre line profiles for $v_x(-1.5,y,0), v_x(2.5,y,0), H_x(-1.5,y,0)$ and $H_x(2.5,y,0)$, for $-2 \leqslant y \leqslant 2$, such that they represent the x-components of the flow field and magnetic field just before and just after the inclusion with $\mu_{rin} = 0.01, 0.1, 1, 10$, in turn. Fig. 16(a) and (b) shows the centreline profiles for v_x and Fig. 16(c) and (d) shows the centre line profile for H_x. In these plots, the effects of including the sphere droplet and increasing permeability contrast can clearly be observed. Note that despite that $\mu_r^{(1)} = \mu_r^{(2)} = 0$ in both fluids the distribution of $[[\mu_r]]$ is still dependent on the strain rate for this problem.

The streamlines, which show the influence of the magnetic fields on the fluid pattern, are shown in Fig. 17 for different values of μ_{rin}. From Fig. 17(c), when there is no contrast between the inner and background fluid, the flow pattern tends to that of the prescribed Poiseuille flow. However, with the presence of a permeability contrast, the flow pattern around the droplet is greatly affected by the magnetic field. This simple example illustrates that the gradient of the permeability, which forms an important role in magnetostriction, also plays a major role for the multiphase MHD problem. In order to resolve these complex flow patterns an hp-finite element scheme is essential without it such complex phenomena observed in this simulation cannot be recovered.

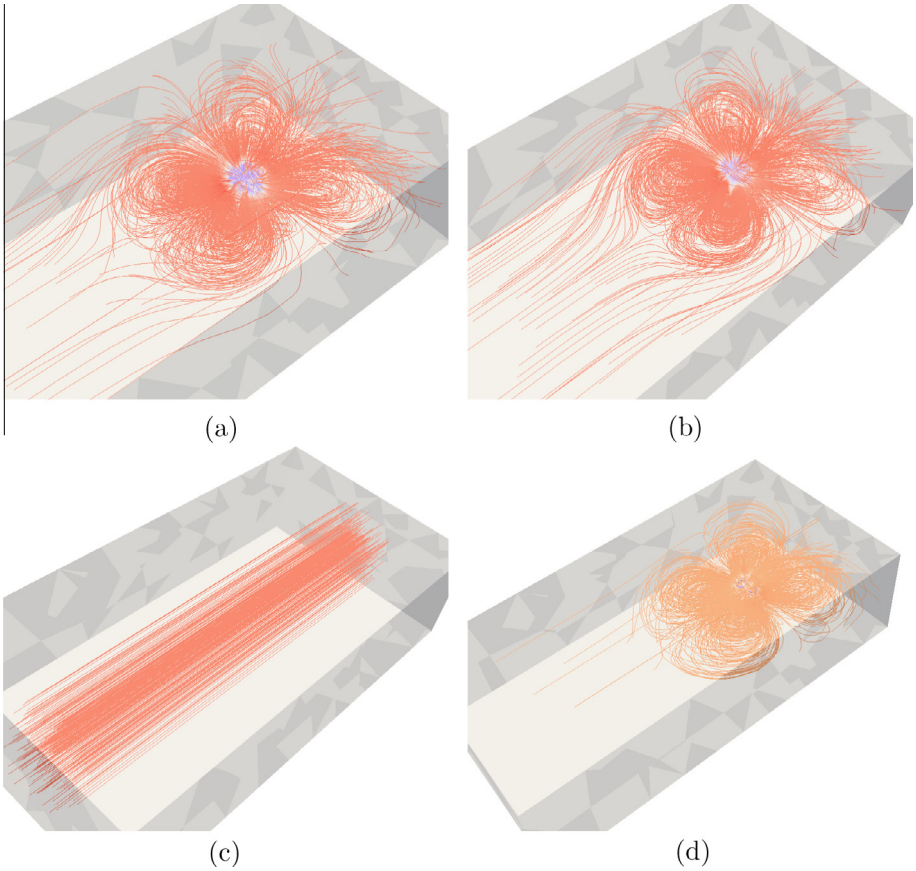

Fig. 17. Three-dimensional multiphase duct flow problem showing: (a)–(d) streamlines for different material properties for inside sphere: $\mu_{rin} = 0.01, 0.1, 1, 10$, respectively.

6. Conclusions

In this paper, we have extended our previous work [25,26] on the numerical simulation of two-dimensional non-conducting magnetostrictive fluids to the simulation of two- and three-dimensional conducting magnetostrictive fluids as well as multi-phase MHD problems. The coupled formulation is implemented in a monolithic manner and solved by means of a Newton–Raphson strategy in conjunction with consistent linearisation. A finite element discretisation employing *hp*-finite elements conforming to the spaces $\boldsymbol{H}(\mathrm{curl}), H^1$ and L_2 has been used leading to a non-trivial implementation. By the application of *p*-refinement, exponential convergence for problems with smooth benchmark solutions has been obtained, and by combining *h*- and *p*-refinements, exponential convergence for benchmark solutions with singularities due to sharp corners and edges has also been demonstrated. We have included further problems that show the predictive capability of the approach and the complex flow patterns that result in the presence of non-homogenous materials and the presence of magnetostrictive effects. Further work will include reducing the computational cost of our approach as well as exploring the role that magnetostriction plays in three dimensional MHD problems in greater detail.

Acknowledgements

The first author gratefully acknowledge the support of the College of Engineering, Swansea University in terms of a Zienkiewicz PhD studentship and the second author gratefully acknowledges the financial support received from EPSRC – United Kingdom in the form of the Grant EP/K023950/1. The third author acknowledges the support received through "The Leverhulme Prize" awarded by The Leverhulme Trust, UK.

References

[1] Armero F, Simo JC. Long-term dissipativity of time-stepping algorithms for an abstract evolution equation with applications to the incompressible MHD and Navier–Stokes equations. Comput Methods Appl Mech Eng 1996;131:41–90.
[2] Aydin SH, Nesliturk AI, Tezer-Sezgin M. Two-level finite element method with a stabilizing subgrid for the incompressible MHD equations. Int J Numer Methods Fluids 2010;62(2):188–210.
[3] Busse FH. Magnetohydrodynamics of the earth's dynamo. Ann Rev Fluid Mech 1978;10(1):435–62.
[4] Cai W, Wu J, Xin J. Divergence-free **H**(div)-conforming hierarchical bases for magnetohydrodynamics (MHD). Commun Math Stat 2013;1(1):19–35.
[5] Codina R, Hernández-Silva N. Stabilized finite element approximation of the stationary magneto-hydrodynamics equations. Comput Mech 2006;38(4–5):344–55.
[6] Davidson PA. An introduction to magnetohydrodynamics, vol. 25. Cambridge University Press; 2001.
[7] Demkowicz L. Computing with hp-adaptive finite elements: volume 1: one and two dimensional elliptic and Maxwell problems. Boca Raton (FL, USA): Chapman and Hall; 2007.
[8] Demkowicz L, Kurtz J, Pardo D, Paszynski M, Rachowicz W, Zdunek A. Computing with hp-adaptive finite elements: volume 2: frontiers: three dimensional elliptic and Maxwell problems with applications. Boca Raton (FL, USA): Chapman and Hall; 2007.
[9] Dong X, He Y, Zhang Y. Convergence analysis of three finite element iterative methods for the 2D/3D stationary incompressible magnetohydrodynamics. Comput Methods Appl Mech Eng 2014;276:287–311.
[10] Dulikravich GS, Lynn SR. Electro-magneto-hydrodynamics: (Part 2) A survey of mathematical models. In Developments in rheological flows, vol. 71; 1995. p. 95–69.
[11] Eringen AC, Maugin GA. Electrodynamics of continua I: Foundations and solid media. New York: Springer-Verlag; 1990.
[12] Eringen AC, Maugin GA. Electrodynamics of continua II: Fluids and complex media. New York: Springer-Verlag; 1990.
[13] Gerbeau J-F. Problèmes Mathématiques et Numériques Posés par la Modélisation de L'electrolyse de L'aluminium. PhD thesis, Ecole des Ponts ParisTech; 1998.
[14] Gerbeau J-F. A stabilized finite element method for the incompressible magnetohydrodynamic equations. Numer Math 2000;87(1):83–111.
[15] Gerbeau J-F, Le Bris C, Lelièvre T. Mathematical methods for the magnetohydrodynamics of liquid metals. Oxford University Press; 2006.
[16] Gerbeau J-F, Lelièvre T, Le Bris C. Simulations of MHD flows with moving interfaces. J Comput Phys 2003;184(1):163–91.
[17] Gil AJ, Ledger PD. A coupled hp-finite element scheme for the solution of two-dimensional electrostrictive materials. Int J Numer Methods Eng 2012;91(11):1158–83.
[18] Greif C, Li D, Schötzau D, Wei X. A mixed finite element method with exactly divergence-free velocities for incompressible magnetohydrodynamics. Comput Methods Appl Mech Eng 2010;199(45–48):2840–55.
[19] Guermond J-L, Minev PD. Mixed finite element approximation of an MHD problem involving conducting and insulating regions: the 2D case. ESAIM: Math Model Numer Anal 2002;36(03):517–36.
[20] Guermond J-L, Minev PD. Mixed finite element approximation of an MHD problem involving conducting and insulating regions: the 3D case. Numer Methods Part Diff Eq 2003;19(6):709–31.
[21] Hasler U, Schneebeli A, Schötzau D. Mixed finite element approximation of incompressible MHD problems based on weighted regularization. Appl Numer Math 2004;51(1):19–45.
[22] Horiuchi R, Sato T. Three-dimensional self-organization of a magnetohydrodynamic plasma. Phys Rev Lett 1985;55(2):211.
[23] Houston P, Schötzau D, Wei X. A mixed DG method for linearized incompressible magnetohydrodynamics. J Sci Comput 2009;40(1–3):281–314.
[24] Jin D. An hp-finite element computational framework for nonlinear magneto-fluid problems including magnetostriction. PhD thesis, Swansea University; 2015.
[25] Jin D, Ledger PD, Gil AJ. An hp-FEM framework for the simulation of coupled magneto-fluid effects. In Proceedings of the 22nd UK conference of the association for computational mechanics in engineering. University of Exeter; 2014. p. 222–5.
[26] Jin D, Ledger PD, Gil AJ. An hp-FEM framework for the simulation of electrostrictive and magnetostrictive materials. Comput Struct 2014;133:131–48.
[27] Jin D, Ledger PD, Gil AJ. An hp-FEM framework for the simulation of stationary incompressible magnetohydrodynamics with magnetostrictive effects in three dimensions. In Proceedings of the 23nd UK conference of the Association for Computational Mechanics in Engineering, Swansea University; 2015.
[28] Kolesnikov Y, Karcher C, Thess A. Lorentz force flowmeter for liquid aluminum: laboratory experiments and plant tests. Metall Mater Trans B 2011;42(3):441–50.
[29] Landau LD, Lifschitz EM, Pitaevskii LP. Electrodynamics of continuous media. 2nd ed. Oxford: Pergamon; 1984.
[30] Moreau R. Magnetohydrodynamics. Dordrecht: Springer-Science+Business Media, B.V.; 1990.
[31] Morley NB, Smolentsev S, Barleon L, Kirillov IR, Takahashi M. Liquid magnetohydrodynamics—recent progress and future directions for fusion. Fusion Eng Des 2000;51:701–13.
[32] Poya R, Gil AJ, Ledger PD. A computational framework for the analysis of linear piezoelectric beams using hp-FEM. Comput Struct 2015;152:155–72.
[33] Rieutord M. Magnetohydrodynamics and solar physics. Available from: arXiv:1410.3725; 2014.
[34] Schneebeli A, Schötzau D. Mixed finite elements for incompressible magneto-hydrodynamics. CR Math 2003;337(1):71–4.
[35] Schöberl J, Zaglmayr S. High order Nédélec elements with local complete sequence properties. Int J Comput Math Electr Electron Eng (COMPEL) 2005;24:374–84.
[36] Schötzau D. Mixed finite element methods for stationary incompressible magneto-hydrodynamics. Numer Math 2004;96(October):771–800.
[37] Schwab C. p- and hp-Finite element methods: theory and applications in solid and fluid mechanics. Oxford: Oxford University Press; 1998.
[38] Stratton JA. Electromagnetic theory. 1st ed. New York: McGraw-Hill Book Company; 1941.
[39] Wong KL, Baker AJ. A 3D incompressible Navier–Stokes velocity–vorticity weak form finite element algorithm. Int J Numer Methods Fluids 2002;38(2):99–123.
[40] Zaglmayr S. High order finite element methods for electromagnetic field computation. PhD thesis, Institut für Numerische Mathematik, Johannes Kepler Univerität Linz, Austria; 2006.
[41] Zhang J, Ni M. Direct simulation of multi-phase MHD flows on an unstructured cartesian adaptive system. J Comput Phys 2014;270:345–65.